Supplement of Atmos. Chem. Phys., 26, 3567–3587, 2026
https://doi.org/10.5194/acp-26-3567-2026-supplement

Atmospheric Chemistry and Physics Open Access

Supplement of

Determining the key sources of uncertainty in dimethyl sulfide and methanethiol oxidation under tropical, temperate, and polar marine conditions

Lorrie S. D. Jacob et al.

Correspondence to: Lorrie S. D. Jacob (lj384@cam.ac.uk) and Alexander T. Archibald (ata27@cam.ac.uk)

S1 Addition of aqueous, halogen and methanethiol chemistry

To explore the effect of halogens, the reactions of DMS, DMSO, and SO with BrO have been included based on the recommended rate constants from the 2019 NASA panel report. The reactions of DMS with Cl atoms have also been included based on the NASA panel report where available; the decomposition of CH_3SClCH_3 uses an indirect measurement by Enami et al. (2004), and the reaction of CH_3SClCH_3 with oxygen uses a rate constant a factor of 10 lower than the upper limit (Urbanski and Wine, 1999), as that reaction has not been observed. Reactions of CH_3SH with OH, NO_3, BrO and Cl using recommendations from the NASA panel report were also included. The full gas-phase mechanism used in this work can be found in Table S2.

Although recent theoretical work indicates that HPMTF undergoes isomerisation to thioperhemiacetal (TPHAC) in the aqueous-phase (Vereecken et al., 2025), for simplicity, in our model HPMTF was immediately converted to sulfate once in the aqueous-phase, as suggested by experimental work from Jernigan et al. (2024). The phase transfer and aqueous-phase acid equilibrium of thioperformic acid (S=CHOOH, TPA) were included using MSA properties and rate constants (a sulfur-based acid whose parameters have been measured or calculated).

To simplify our model, we did not include halogen aqueous reactions. The reaction of MSI^- (the MSIA ion) with Cl_2^- could contribute around 10% of aqueous MSIA oxidation, and the oxidation product, CH_3SO_2OO(aq), can react with MSIA again; the initial reaction with Cl_2^- can result in the loss of two aqueous MSIA molecules (Hoffmann et al., 2016). Although our analysis focuses on gas-phase concentrations, the omission of aqueous halogen reactions may affect the results by increasing the concentration of gas-phase MSIA (and subsequent oxidation products, gas-phase SO_2, MSA and H_2SO_4) through the omission of an aqueous sink. However, the major aqueous oxidation pathway of MSIA (reaction of MSIA with O_3, Hoffmann et al. (2016)), has been included in our mechanism.

Accommodation coefficients, gas-phase diffusion coefficients and Henry's law constants used in this work and their sources are given in Table S1. Additionally, the uncertainty factors for Henry's law constants are provided in the table (see Section S10 for more information on the determination of those uncertainties). When there was no measured gas-phase diffusion coefficient available, it was calculated using the Fuller method using parameters from Tang et al. (2014).

The aqueous reactions and phase transfers were implemented into BOXMOX (Knote and Barre, 2022), a KPP wrapper (Sandu and Sander, 2006), using the same methodology as the SPACCIM model (Wolke et al., 2005). To ensure they had been implemented correctly, the modelling work by Hoffmann et al. (2016) was replicated by constraining pH, liquid water content and oxidants to their modelled data, which is shown in the Section S1.1.

S1.1 Implementation of aqueous chemistry

To incorporate aqueous chemistry, the microphysics used in SPACCIM (Wolke et al., 2005) for a mono-dispersed aerosol/cloud droplet was used. This implementation assumes a homogeneous, dilute water droplet, however, it has also been used for deliquesced particles (Hoffmann et al., 2016). The particle radius was kept constant for simplicity, as in Hoffmann et al. (2016).

Table S1. The accommodation coefficient (α), gas-phase diffusion coefficient (D_g, $cm^2\ s^{-1}$), Henry's law constant at 298 K (H_{298K}, $M\ atm^{-1}$), uncertainty factor attributed to Henry's law constant ($f^2(T)$) and temperature dependence of Henry's law constant ($-\Delta H_{sol}/R$, K) for the species included in our model, along with their sources. The calculated gas-diffusion coefficients are derived from the Fuller method, using parameters from Tang et al. (2014).

	α	Reference	D_g	Reference	H_{298K}	$f^2(T)$	Reference	$-\Delta H_{sol}/R$	Reference
DMS	0.001	a	0.105	Calculated	0.54	55	b	3460	b
DMSO	0.06	c	0.098	Calculated	9.9×10^4	55	b	1330	d
DMSO2	0.05	c	0.093	Calculated	1.18×10^6	55	e	5390	f
MSA	0.1	c	0.079	g	1.13×10^8	55	e	1760	f
MSIA	0.1	as for MSA	0.107	Calculated	1.69×10^6	55	e	1760	as for MSA
H_2SO_4	1	h	0.097	g	inf		f		
SO_2	0.2	i	0.123	g	1.36	1.3	b	4250	b
TPA	0.1	as for MSA	0.111	Calculated	1.18×10^6	100	as for MSA	1760	as for MSA
HPMTF	0.006	as for CH_3OOH (j)	0.091	Calculated	inf		k		
CH_3SH	0.001	as for DMS	0.127	Calculated	0.39	55	b	3420	b
O_3	0.1	b	0.179	Calculated	1.03×10^{-2}	1.3	b	2830	b
HO_2	1	b	0.208	Calculated	690	6	b		
H_2O_2	0.18	b	0.153	g	8.7×10^4	1.75	b	7290	b
O_2	0.01	l	0.202	g	1.27×10^{-3}	1.1	b	8160	b

References: a Zhu et al. (2006), b Burkholder et al. (2019), c De Bruyn et al. (1994), d Watts and Brimblecombe (1987), e Wollesen de Jonge et al. (2021), f Campolongo et al. (1999), g Tang et al. (2014), h Hanson (2005), i Boniface et al. (2000), j Magi et al. (1997), k Jernigan et al. (2024), l Ervens et al. (2003)

The phase transfer rate for a species, X, from the gas-phase to the aqueous-phase (adsorption, A) was given by:

$$A = \frac{L}{\frac{r^2}{3D_\mathrm{g}} + \frac{4r}{3\bar{v}\alpha}}$$

where L is the unitless liquid water content in the box (due to aerosols or clouds), r is the radius of the cloud droplet or aerosol (m), D_g is the gas diffusion coefficient of X ($\mathrm{m^2\ s^{-1}}$), α is the mass accommodation coefficient (unitless) of X and $\bar{v}$ is the mean molecular velocity ($\mathrm{m\ s^{-1}}$),

$$\bar{v} = \sqrt{\frac{8\mathrm{R}T}{\pi M}}$$

with R as the gas constant (8.3145 J $\mathrm{K^{-1}\ mol^{-1}}$), T as temperature (K) and M as molecular weight of X ($\mathrm{kg\ mol^{-1}}$).

The phase transfer rate for species X from aqueous-phase to gas-phase (desorption, D) was given by:

$$D = \frac{A}{LH_T}$$

where H_T is Henry's law coefficient for X (unitless),

$$H_T = H_{298\mathrm{K}}\mathrm{R}T\mathrm{e}^{\frac{-\Delta H_\mathrm{sol}}{\mathrm{R}}(\frac{1}{T}-\frac{1}{298})}$$

with $H_{298\mathrm{K}}$ as Henry's law coefficient of X at 298 K ($\mathrm{mol\ L^{-1}\ atm^{-1}}$), ΔH_sol the enthalpy of dissolution ($\mathrm{mol\ L^{-1}\ atm^{-1}}$) and R the gas constant (0.082057 L atm $\mathrm{K^{-1}\ mol^{-1}}$).

In our box model, the concentrations of species are given in molecules $\mathrm{cm^{-3}}$, however, first-order rate constants for aqueous reactions are typically given in L $\mathrm{mol^{-1}\ s^{-1}}$. Additionally, for bimolecular reactions, the fraction of water in the box (liquid water content, L) has to be taken into account. As such, aqueous-phase first-order rate constants are converted to $\mathrm{cm^3}$ molecules^{-1} $\mathrm{s^{-1}}$, and divided by L. For reactions involving water, a concentration of 55.6 mol $\mathrm{L^{-1}}$ is used. The concentration of hydrogen ions, $[\mathrm{H^+}]$ was constrained based on observations.

In order to ensure that the microphysics had been correctly implemented into BOXMOX, box model simulations by Hoffmann et al. (2016) were replicated. The implementation of the full CAPRAM mechanism, including halogen chemistry, was outside of the scope of this work. Instead, the output concentrations of oxidants from Hoffmann et al. (accessed through correspondence), were used, which included concentrations of $\mathrm{Cl(g)}$, $\mathrm{ClO(g)}$, $\mathrm{BrO(g)}$, $\mathrm{Cl^-(aq)}$, $\mathrm{Cl_2^-(aq)}$, $\mathrm{OH(aq)}$, $\mathrm{O_3(aq)}$. Additionally, emissions, deposition velocities, initial concentrations, pH, particle/droplet radius, liquid water content, zenith angle (for photolysis rates) and temperature were constrained. Our modelled results are shown in Figure S1, which closely replicate Figures S3, S6, S8 and S10 from the Hoffmann et al. (2016) supporting information.

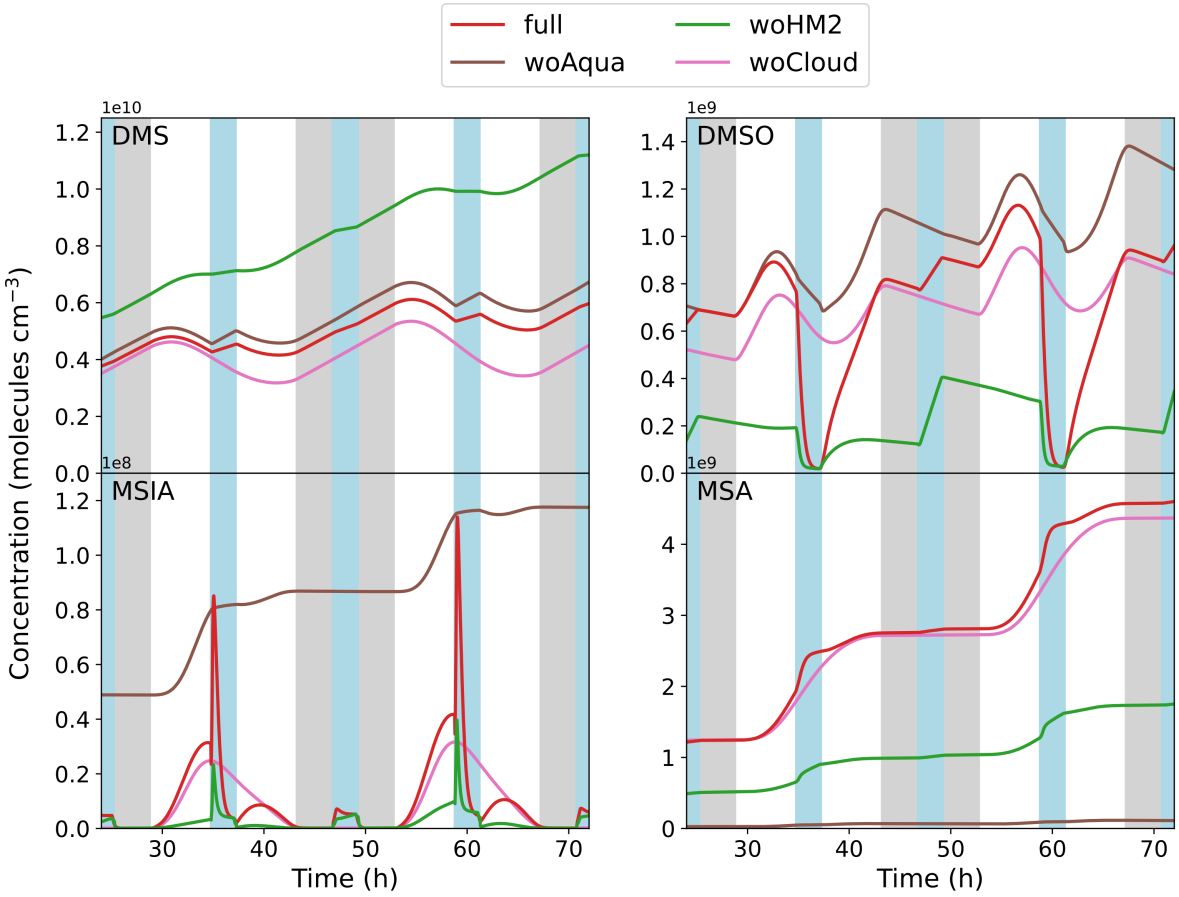

Figure S1. The concentration of DMS, DMSO, MSIA and MSA modelled in this work, replicating the modelling from Hoffmann et al. (2016). The coloured lines represent sensitivity runs used by Hoffmann et al., the grey bars represent the night periods, and the blue bars represent cloud periods.

S2 Updates to dimethyl sulfide mechanism

The equilibrium rate constants for CH_3SO and CH_3SO_2 reacting with oxygen calculated theoretically by Chen et al. (2023) have been included; previously these rate constants were based on structure-activity relationships. To be consistent with our methodology of using evaluated kinetic data where possible, we rescaled the equilibrium constants from Chen et al. (2023) using the NASA panel report data for the reaction between CH_3S and O_2 (1.7×10^{-19} cm^3 molecule^{-1} s^{-1} at 298 K), and the temperature-dependent equilibrium rate constant for the reaction of CH_3S and O_2 from the report was also used in the updated mechanism. Additionally, the decomposition of CH_3SO_2, along with CH_3SOO isomerisation into CH_3SO_2 (which subsequently decomposes), from Chen et al. (2023) have been added.

Berndt (2025) recently investigated the reaction of CH_3SO_3 with H donors to form methanesulfonic acid (CH_3SO_3H, MSA), and determined that the reaction of HO_2 with CH_3SO_3 is a minor reaction. In the supplementary of the Berndt (Figure S2) the modelled concentration of HO_2 is given, along with the measured [MSA]/[SO_3] ratio (Berndt, 2025). From the rate constants at 298 K, we can estimate an expected [MSA]/[SO_3] ratio and compare it to what was measured. In the Berndt paper, when the NO concentration was around 2×10^{10} molecules cm^{-3}, the modelled HO_2 concentration was 1.8×10^9 molecules cm^{-3}. According to that paper, the decomposition of CH_3SO_3 to form SO_3 has a rate constant of $5.4\times10^{12} \times e^{-9411/T}$ s^{-1}, and at 298 K, the first-order rate constant is 0.10 s^{-1}. The rate constant estimated by Yin et al. (1990) for the reaction of CH_3SO_3 and HO_2 was 5.0×10^{-11} cm^3 molecules^{-1} s^{-1}. At 298 K, the estimated ratio is

$$\frac{[\text{MSA}]}{[SO_3]} = \frac{k_{CH_3SO_3 + HO_2} \times [HO_2]}{k_{CH_3SO_3 \text{ decomp}}} = \frac{5\times10^{-11}\times1.8\times10^9}{0.10} = 0.9$$

This is higher than the measured ratio of 0.2 at the same concentrations. A reduction of $k_{CH_3SO_3 + HO_2}$ by a factor of 5 would reproduce this measured ratio; we therefore treat this value as an upper limit for the rate constant under experimental conditions. Decreasing the rate constant by a factor of 50 provides a ratio of 0.02, which is below this upper limit, and accounts for other possible H donors in the experiment. $HCHO$, DMSO and MSIA (potential H donors) are present in the experiment; although there is no evidence that they will act as H donors, CH_3SH and CH_3SSCH_3 have been found to act as H donors to CH_3SO_3 (Berndt et al., 2023), along with DMS (Jacob et al., 2024). To account for the work from Berndt (2025), the rate constant for the reaction of CH_3SO_3 and HO_2 was decreased by a factor of 50 and an uncertainty factor of 10 was applied, such that the upper limit is explored in the uncertainty propagation. The temperature-dependent decomposition rate constant for CH_3SO_3 recommended by Berndt (2025) was also updated in our mechanism.

Finally, Goss and Kroll (2024) studied the OH-initiated oxidation of dimethyl sulfoxide (CH_3SOCH_3, DMSO), and found that dimethyl sulfone ($CH_3SO_2CH_3$, DMSO2) was not produced. They suggested that DMSO2 was measured in chambers that included higher mixing ratios of DMSO (> 1 ppm), due to increased RO_2 reactions. To account for DMSO2 not being measured in a chamber with lower RO_2 concentrations, which is more representative of marine conditions, the formation of DMSO2 from the reaction of OH and DMSO (that had not been validated) was removed in the updated mechanism, with the reaction now solely forming methanesulfinic acid (CH_3SO_2H, MSIA).

S3 Evaluation of the updated mechanism

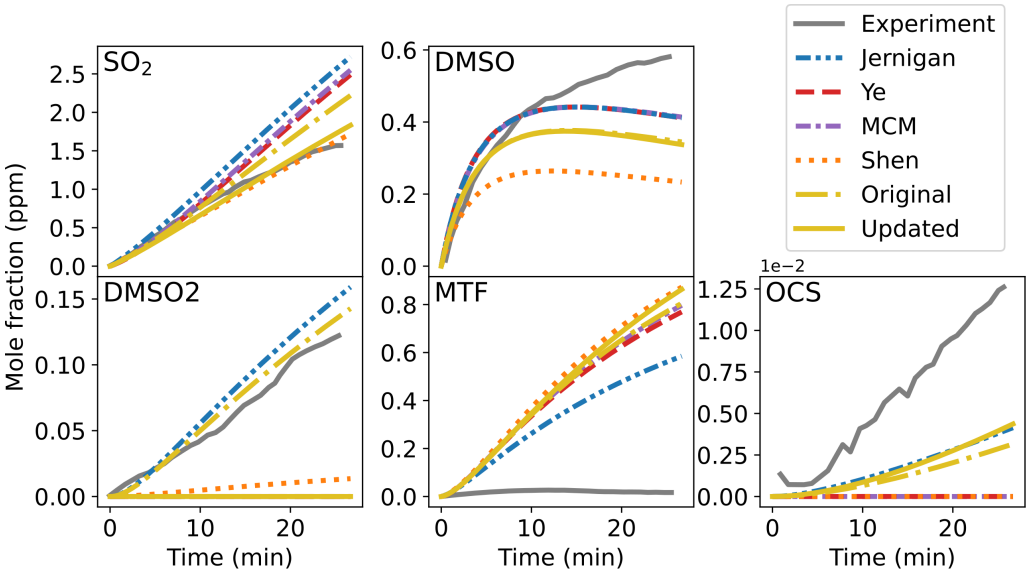

Figure S2. The products measured in the Albu et al. (2008) experiment, compared to the modelling results from the Jernigan, Ye, MCM and Shen mechanisms, along with the original mechanism from Jacob et al. (2024), and the updated mechanism used in this work. Note that the original mechanism can only be seen when it deviates from the updated mechanism.

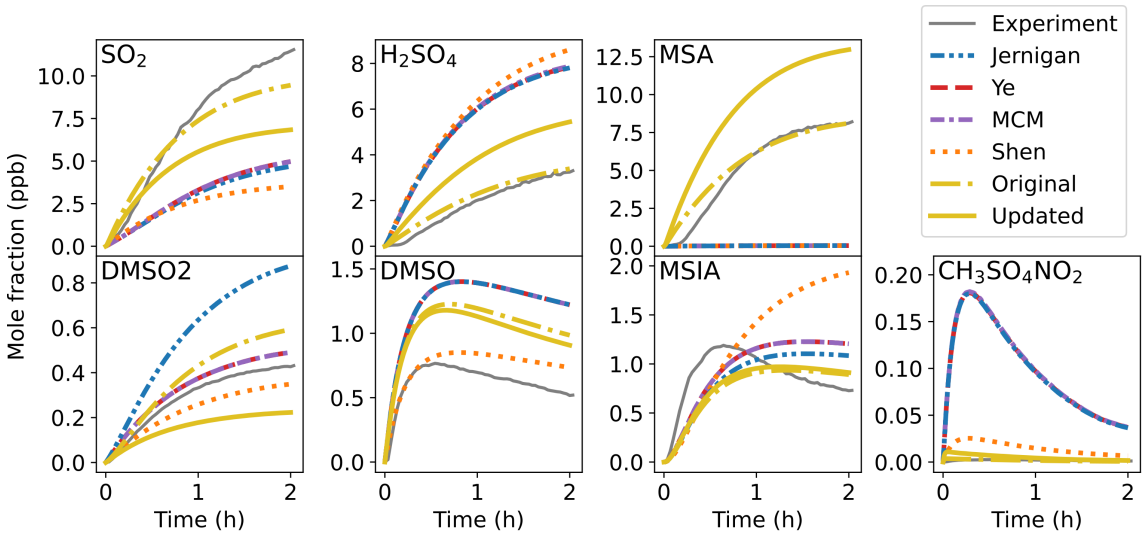

Figure S3. The products measured in the Ye et al. (2022) experiment 1, compared to the modelling results from the Jernigan, Ye, MCM and Shen mechanisms, along with original mechanism from Jacob et al. (2024), and the updated mechanism used in this work. Note that the original mechanism can only be seen when it deviates from the updated mechanism. Additionally, the experimental DMSO2 represents the product $C_2H_6SO_2$ measured by Ye et al., which may also include CH_3SCH_2OOH.

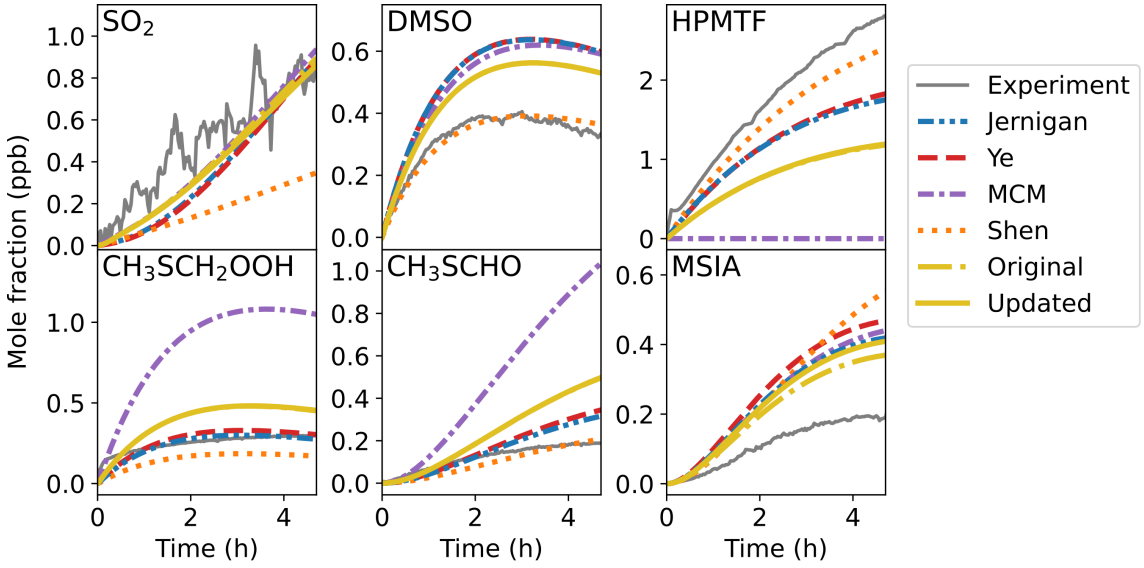

Figure S4. The products measured in the Ye et al. (2022) experiment 2a, compared to the modelling results from the Jernigan, Ye, MCM and Shen mechanisms, along with original mechanism from Jacob et al. (2024), and the updated mechanism used in this work. Note that the original mechanism can only be seen when it deviates from the updated mechanism. Additionally, the experimental CH_3SCH_2OOH represents the product $C_2H_6SO_2$ measured by Ye et al. (2022), which may also include DMSO2.

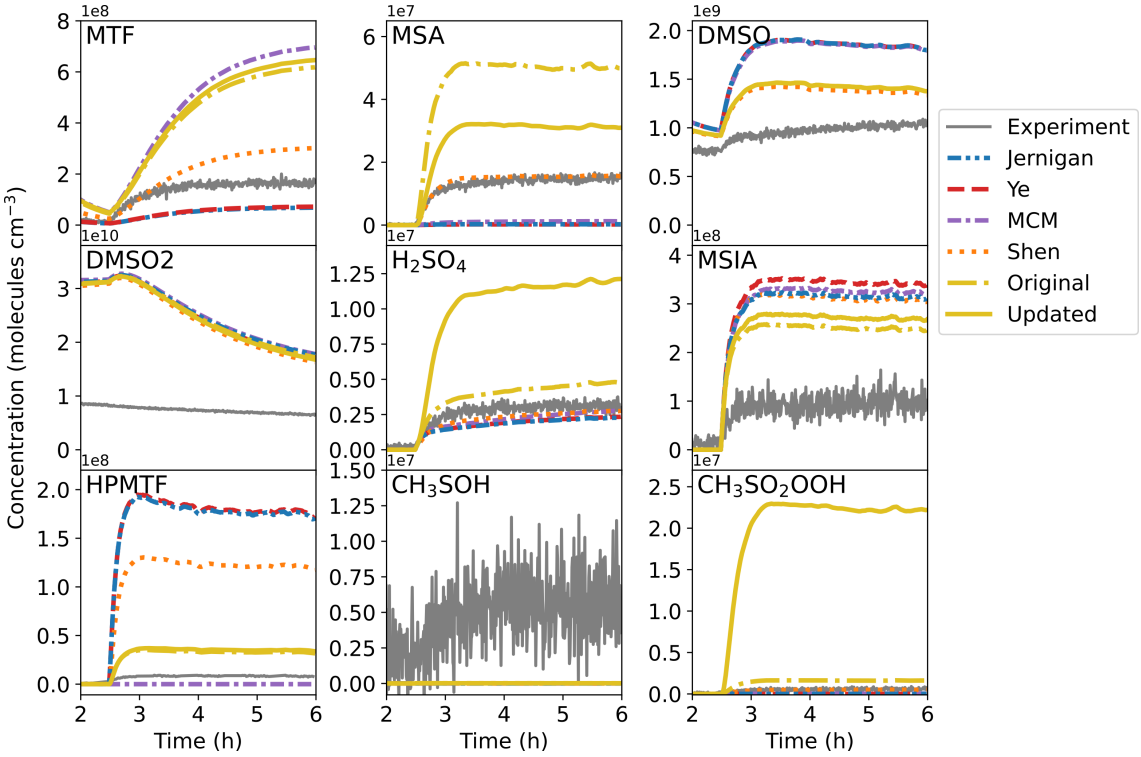

Figure S5. The products measured in the Shen et al. (2022) experiment, compared to the modelling results from the Jernigan, Ye, MCM and Shen mechanisms, along with original mechanism from Jacob et al. (2024), and the updated mechanism used in this work. Note that the original mechanism can only be seen when it deviates from the updated mechanism.

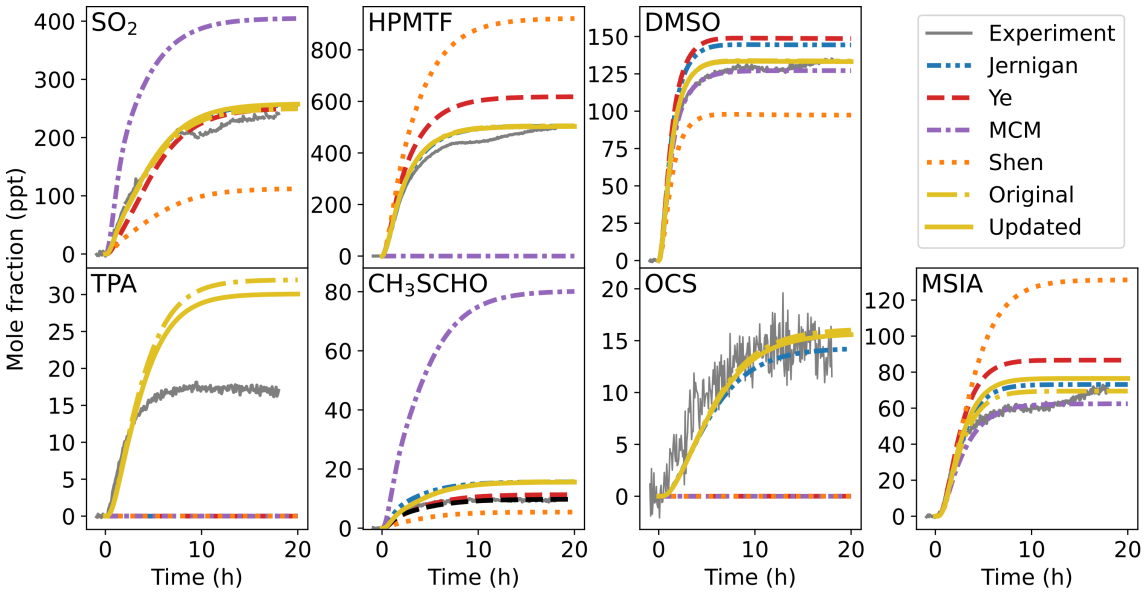

Figure S6. The products measured in the Jernigan et al. (2022) experiment, compared to the modelling results from the Jernigan, Ye, MCM and Shen mechanisms, along with the original mechanism from Jacob et al. (2024), and the updated mechanism used in this work. Note that the original mechanism can only be seen when it deviates from the updated mechanism.

S4 Updated mechanism with uncertainty factors

The updated gas-phase mechanism used in this work, including the rate constants and the uncertainty factors for each reaction is shown in Table S2. The reactions and rate constants that have been updated compared to the original mechanism from Jacob et al. (2024) are shown in bold. As with the Master Chemical Mechanism, the formation of H_2O, O_2 and CO_2 are not included. The halogen reactions were included offline for this work, and as such, Cl and Br are not conserved in this mechanism.

Table S2: The reactions, rate constants, uncertainty factors at 298 K (f^2(298 K)), temperature dependence in the uncertainty factor (g), and the source of the rate constants. Only references for reactions that have been added or adjusted in this update are included, for further references see Jacob et al. (2024)

	Reaction	Rate constant	f^2(298 K)[a]	g	Source
1	$CH_3S + NO_2 \rightarrow CH_3SO + NO$	$3 \times 10^{-11} \times e^{(240/T)}$	1.44	150	Evaluated
2	$CH_3S + O_3 \rightarrow CH_3SO$	$1.5 \times 10^{-12} \times e^{(360/T)}$	1.32	100	Evaluated
3	$CH_3S \rightarrow CH_3SOO$	$1.20 \times 10^{-16} \times e^{(1580/T)} \times [O_2]$	1.44		Evaluated
4	$CH_3SCHO + OH \rightarrow CH_3S + CO$	1.23×10^{-11}	1.5		Direct
5	$CH_3SCHO \rightarrow CH_3S + CO + HO_2$	J("C3H7CHO")	10		SAR
6	$CH_3SCH_2O \rightarrow CH_3S + HCHO$	KDEC	10		SAR
7	$CH_3SCH_2OH + OH \rightarrow CH_3SCHO + HO_2$	2.78×10^{-11}	10		SAR
8	$CH_3SCH_2OOH + OH \rightarrow CH_3SCHO + OH$	7.03×10^{-11}	10		SAR
9	$CH_3SCH_2OOH \rightarrow CH_3SCH_2O + OH$	J("CH3OOH")	10		SAR
10	$CH_3SCH_2OONO_2 \rightarrow CH_3SCH_2O_2 + NO_2$	0.134	10		SAR
11	$CH_3SCH_2O_2 + HO_2 \rightarrow CH_3SCH_2OOH$	KRO2HO2 $\times$ 0.387	10		SAR
12	$CH_3SCH_2O_2 + NO_2 \rightarrow CH_3SCH_2OONO_2$	9.20×10^{-12}	3.2		Evaluated[b]
13	$CH_3SCH_2O_2 + NO_3 \rightarrow CH_3SCH_2O + NO_2$	KRO2NO3	10		SAR
14	$CH_3SCH_2O_2 + NO \rightarrow CH_3SCH_2O + NO_2$	$4.9 \times 10^{-12} \times e^{(260/T)}$	1.69	200	Evaluated
15	$CH_3SCH_2O_2 \rightarrow CH_3SCH_2O$	$3.74 \times 10^{-12} \times [RO_2] \times 0.8$	3		Indirect[c]
16	$CH_3SCH_2O_2 \rightarrow CH_3SCH_2OH$	$3.74 \times 10^{-12} \times [RO_2] \times 0.1$	3		Indirect[c]
17	$CH_3SCH_2O_2 \rightarrow CH_3SCHO$	$3.74 \times 10^{-12} \times [RO_2] \times 0.1$	3		Indirect[c]

18	$CH_3SCH_2O_2 \rightarrow HOOCH_2SCH_2O_2$	$2.39 \times 10^9 \times e^{(-7278/T)}$	2		Direct
19	$\mathbf{CH_3SClCH_3 + NO_2 \rightarrow DMS + NO_2}$	$\mathbf{2.7 \times 10^{-11}}$	1.56		Evaluated[1]
20	$\mathbf{CH_3SClCH_3 + NO \rightarrow DMS + NO}$	$\mathbf{1.2 \times 10^{-11}}$	1.56		Evaluated[1]
21	$\mathbf{CH_3SClCH_3 \rightarrow DMSO}$	$\mathbf{4.0 \times 10^{-19} \times [O_2]}$	10		Estimate[d]
22	$\mathbf{CH_3SClCH_3 \rightarrow DMS}$	**90**	3		Indirect[2]
23	$\mathbf{CH_3SH + OH \rightarrow CH_3S}$	$\mathbf{9.9 \times 10^{-12} \times e^{(360/T)}}$	1.14	75	Evaluated[1]
24	$\mathbf{CH_3SH + NO_3 \rightarrow CH_3S + HNO_3}$	$\mathbf{4.4 \times 10^{-13} \times e^{(210/T)}}$	1.56	200	Evaluated[1]
25	$\mathbf{CH_3SH + BrO \rightarrow CH_3S}$	$\mathbf{2.2 \times 10^{-15} \times e^{(830/T)}}$	10		Direct[3]
26	$\mathbf{CH_3SH + Cl \rightarrow CH_3S}$	$\mathbf{1.2 \times 10^{-10} \times e^{(150/T)}}$	1.21	100	Evaluated[1]
27	$CH_3SO + NO_2 \rightarrow CH_3O_2 + SO_2 + NO$	$1.20 \times 10^{-11} \times 0.25$	1.64		Direct[e]
28	$CH_3SO + NO_2 \rightarrow CH_3SO_2 + NO$	$1.20 \times 10^{-11} \times 0.75$	1.51		Direct[e]
29	$CH_3SO + O_3 \rightarrow CH_3O_2 + SO_2$	4.00×10^{-13}	2.25		Evaluated
30	$CH_3SO \rightarrow CH_3SOO_2$	$3.12 \times 10^{-16} \times e^{(1580/T)} \times [O_2]$	5		Theory
31	$CH_3SO4NO_2 + OH \rightarrow CH_3SO_2O_2 + HNO_3$	3.60×10^{-13}	10		SAR
32	$CH_3SO4NO_2 \rightarrow CH_3SO_2O_2 + NO_2$	0.134	[f]		Indirect
33	$CH_3SOH + O_3 \rightarrow CH_3O_2 + HO_2 + SO_2$	2.00×10^{-12}	3		Indirect
34	$CH_3SOH + OH \rightarrow CH_3SO$	5.00×10^{-11}	10		Estimate
35	$CH_3SOHCH_3 \rightarrow CH_3SOH + CH_3O_2$	5.00×10^5	10		Estimate
36	$CH_3SOHCH_3 \rightarrow DMS + OH$	KDMSOH	[f]		Evaluated
37	$CH_3SOHCH_3 \rightarrow HODMSO2$	$8.5 \times 10^{-13} \times [O_2]$	1.56	0	Evaluated
38	$CH_3SOO + HO_2 \rightarrow CH_3SOOH$	4.00×10^{-12}	10		SAR
39	$CH_3SOO + NO_2 \rightarrow CH_3SO + NO_3$	2.2×10^{-11}	2	100	Evaluated
40	$CH_3SOO + NO \rightarrow CH_3SO + NO_2$	1.1×10^{-11}	2	100	Evaluated
41	$CH_3SOO \rightarrow CH_3O_2 + SO_2$	**KRSOOisom**	5	0	Theory[4]
42	$CH_3SOO \rightarrow CH_3S$	**KRSOOb**	[f]		Evaluated[1]
43	$CH_3SOOH + OH \rightarrow CH_3SOO$	$3.68 \times 10^{-13} \times e^{(635/T)}$	10		SAR
44	$CH_3SOOH \rightarrow CH_3SO + OH$	J("CH3OOH")	10		SAR
45	$CH_3SOOOH + OH \rightarrow CH_3SOO_2$	9.00×10^{-11}	10		SAR
46	$CH_3SOOOH \rightarrow CH_3SO_2 + OH$	J("CH3OOH")	10		SAR
47	$CH_3SOO_2 + HO_2 \rightarrow CH_3SO_2 + OH$	KAPHO2 $\times$ 0.44	10		SAR

48	$CH_3SOO_2 + HO_2 \rightarrow CH_3SOOOH$	KAPHO2 $\times$ 0.41	10	SAR
49	$CH_3SOO_2 + HO_2 \rightarrow MSIA + O_3$	KAPHO2 $\times$ 0.15	10	SAR
50	$CH_3SOO_2 + NO_2 \rightarrow CH_3SOO_2NO_2$	$1.20 \times 10^{-12} \times (T/300)^{-0.9}$	10	SAR
51	$CH_3SOO_2 + NO_3 \rightarrow CH_3SO_2 + NO_2$	KRO2NO3 $\times$ 1.74	10	SAR
52	$CH_3SOO_2 + NO \rightarrow CH_3SO_2 + NO_2$	1.00×10^{-11}	10	SAR
53	$CH_3SOO_2 \rightarrow CH_3SO$	**KRSOO2b**	*f*	Theory[4]
54	$CH_3SOO_2 \rightarrow CH_3SO_2$	$1.00 \times 10^{-11} \times [RO_2] \times 0.7$	10	SAR
55	$CH_3SOO_2 \rightarrow MSIA$	$1.00 \times 10^{-11} \times [RO_2] \times 0.3$	10	SAR
56	$CH_3SOO_2NO_2 + OH \rightarrow MSIA + NO_2$	1.00×10^{-11}	10	SAR
57	$CH_3SOO_2NO_2 \rightarrow CH_3SOO_2 + NO_2$	0.134	*f*	SAR
58	$CH_3SO_2 + NO_2 \rightarrow CH_3SO_3 + NO$	2.20×10^{-12}	2	Evaluated
59	$CH_3SO_2 + O_3 \rightarrow CH_3SO_3$	3.00×10^{-13}	10	Estimate
60	$CH_3SO_2 + OH \rightarrow MSA$	5.00×10^{-11}	10	Estimate
61	$CH_3SO_2 \rightarrow CH_3O_2 + SO_2$	$\mathbf{1.7 \times 10^{15} \times e^{-8.4 \times 10^3/T} \times e^{1.8 \times 10^6/T^3}}$	5	Theory[4]
62	$CH_3SO_2 \rightarrow CH_3SO_2O_2$	$1.03 \times 10^{-16} \times e^{(1580/T)} \times [O_2]$	5	Theory
63	$CH_3SO_2CHO + OH \rightarrow CH_3SO_2 + CO$	1.78×10^{-12}	10	SAR
64	$CH_3SO_2CHO \rightarrow CH_3SO_2 + CO + HO_2$	J("C3H7CHO")	10	SAR
65	$CH_3SO_2OOH + OH \rightarrow CH_3SO_2O_2$	3.60×10^{-12}	10	SAR
66	$CH_3SO_2OOH \rightarrow CH_3SO_3 + OH$	J("CH3OOH")	10	SAR
67	$CH_3SO_2O_2 + HO_2 \rightarrow CH_3SO_2OOH$	KAPHO2 $\times$ 0.41	10	SAR
68	$CH_3SO_2O_2 + HO_2 \rightarrow CH_3SO_3 + OH$	KAPHO2 $\times$ 0.44	10	SAR
69	$CH_3SO_2O_2 + HO_2 \rightarrow MSA + O_3$	KAPHO2 $\times$ 0.15	10	SAR
70	$CH_3SO_2O_2 + NO_2 \rightarrow CH_3SO4NO_2$	$1.20 \times 10^{-12} \times (T/300)^{-0.9}$	10	SAR
71	$CH_3SO_2O_2 + NO_3 \rightarrow CH_3SO_3 + NO_2$	KRO2NO3 $\times$ 1.74	10	SAR
72	$CH_3SO_2O_2 + NO \rightarrow CH_3SO_3 + NO_2$	1.00×10^{-11}	10	SAR
73	$CH_3SO_2O_2 \rightarrow CH_3SO_2$	**KRSO2O2b**	*f*	Theory[4]
74	$CH_3SO_2O_2 \rightarrow CH_3SO_3$	$1.00 \times 10^{-11} \times [RO_2] \times 0.7$	10	SAR
75	$CH_3SO_2O_2 \rightarrow MSA$	$1.00 \times 10^{-11} \times [RO_2] \times 0.3$	10	SAR
76	$CH_3SO_3 + CH_3OH \rightarrow MSA + HO_2 + HCHO$	1.00×10^{-16}	10	Estimate
77	$CH_3SO_3 + CH_3OOH \rightarrow MSA + CH_3O_2$	3.00×10^{-16}	10	Estimate

78	CH_3SO_3 + DMS → MSA + $CH_3SCH_2O_2$	1.45×10^{-13}	10		Estimate
79	CH_3SO_3 + H_2O_2 → MSA + HO_2	3.00×10^{-16}	10		Estimate
80	CH_3SO_3 + HCHO → MSA + HO_2 + CO	1.60×10^{-15}	10		Estimate
81	CH_3SO_3 + HO_2 → MSA	$\mathbf{1.00 \times 10^{-12}}$	10		Estimate[d]
82	CH_3SO_3 + HONO → MSA + NO_2	6.60×10^{-16}	10		Estimate
83	CH_3SO_3 + MSIA → MSA + CH_3SO_2	1.00×10^{-13}	10		Estimate
84	CH_3SO_3 → CH_3O_2 + SO_3	$\mathbf{5.4 \times 10^{12} \times e^{(-9411/T)}}$	3		Indirect[5]
85	**DMS + BrO → DMSO**	$\mathbf{1.4 \times 10^{-14} \times e^{(950/T)}}$	1.56	200	Evaluated[1]
86	**DMS + Cl → $CH_3SCH_2O_2$**	$\mathbf{9.4 \times 10^{-11} \times e^{(190/T)}}$	1.44	0	Evaluated[1]
87	**DMS + Cl → CH_3SClCH_3**	$\mathbf{3.5 \times 10^{-10} - 9.4 \times 10^{-11} \times e^{190/T}}$	2.37	0	Evaluated[1]
88	DMS + NO_3 → $CH_3SCH_2O_2$ + HNO_3	$1.9 \times 10^{-13} \times e^{(530/T)}$	1.21	150	Evaluated
89	DMS + OH → CH_3SOHCH_3	$[M] \times 3 \times 10^{-31} \times (T/298)^{-6.24}$	1.96	0	Evaluated
90	DMS + OH → $CH_3SCH_2O_2$	$1.2 \times 10^{-11} \times e^{(-280/T)}$	1.21	100	Evaluated
91	DMS + O → CH_3SO + CH_3O_2	$1.3 \times 10^{-11} \times e^{(410/T)}$	1.21	100	Evaluated
92	**DMSO + BrO → DMSO2**	$\mathbf{1 \times 10^{-14}}$	2		Evaluated[1]
93	DMSO + NO_3 → DMSO2 + NO_2	2.90×10^{-13}	2.56		Evaluated
94	DMSO + OH → MSIA + CH_3O_2	$\mathbf{6.1 \times 10^{-12} \times e^{(800/T)}}$	1.44	500	Evaluated[1]
95	DMSO + O → SO_2 + CH_3O_2 + CH_3O_2	$2.0 \times 10^{-12} \times e^{(440/T)}$	1.44	200	Evaluated
96	DMSO2 + OH → DMSO2O2	1.00×10^{-14}	10		Estimate
97	DMSO2O → CH_3SO_2 + HCHO	KDEC	10		SAR
98	DMSO2O2 → CH_3SO_2CHO	$2.00 \times 10^{-12} \times [RO_2] \times 0.2$	10		SAR
99	DMSO2O2 → DMSO2O	$2.00 \times 10^{-12} \times [RO_2] \times 0.6$	10		SAR
100	DMSO2O2 → DMSO2OH	$2.00 \times 10^{-12} \times [RO_2] \times 0.2$	10		SAR
101	DMSO2O2 + HO_2 → DMSO2OOH	KRO2HO2 × 0.387	10		SAR
102	DMSO2O2 + NO_3 → DMSO2O + NO_2	KRO2NO3	10		SAR
103	DMSO2O2 + NO → DMSO2O + NO_2	KRO2NO	10		SAR
104	DMSO2OH + OH → CH_3SO_2CHO + HO_2	5.23×10^{-13}	10		SAR
105	DMSO2OH + OH → DMSO2O	1.40×10^{-13}	10		SAR
106	DMSO2OOH → DMSO2O + OH	J("CH3OOH")	10		SAR
107	DMSO2OOH + OH → CH_3SO_2CHO + OH	1.26×10^{-12}	10		SAR

108	DMSO2OOH + OH → DMSO2O2	3.60×10^{-12}	10	SAR
109	$HOCH_2S + NO_2 \rightarrow HOCH_2SO + NO$	$3.0 \times 10^{-11} \times e^{(240/T)}$	10	SAR
110	$HOCH_2S + O_3 \rightarrow HOCH_2SO$	$1.5 \times 10^{-12} \times e^{(360/T)}$	10	SAR
111	$HOCH_2S \rightarrow HOCH_2SOO$	$1.20 \times 10^{-16} \times e^{(1580/T)} \times [O_2]$	10	SAR
112	$HOCH_2SO + NO_2 \rightarrow HCHO + HO_2 + SO_2 + NO$	1.2×10^{-11}	10	SAR
113	$HOCH_2SO + O_3 \rightarrow HCHO + HO_2 + SO_2$	4.0×10^{-13}	10	SAR
114	$HOCH_2SOO \rightarrow HOCH_2S$	**KRSOOb**	*f*	SAR
115	$HOCH_2SOO \rightarrow HCHO + HO_2 + SO_2$	**KRSOOisom**	10	SAR
116	HODMSO2 → DMSO + HO_2	$8.90 \times 10^{+10} \times e^{(-6040/T)}$	10	SAR
117	HODMSO2 + NO → DMSO2 + HO_2 + NO_2	5.00×10^{-12}	10	SAR
118	$HOOCH_2S + NO_2 \rightarrow HOOCH_2SO + NO$	$3.0 \times 10^{-11} \times e^{(240/T)}$	10	SAR
119	$HOOCH_2S + O_3 \rightarrow HOOCH_2SO$	$1.5 \times 10^{-12} \times e^{(360/T)}$	10	SAR
120	$HOOCH_2S \rightarrow HOOCH_2SOO$	$1.20 \times 10^{-16} \times e^{(1580/T)} \times [O_2]$	10	SAR
121	$HOOCH_2SCH_2O \rightarrow HOOCH_2S + HCHO$	KDEC	10	SAR
122	$HOOCH_2SCH_2OH + OH \rightarrow HPMTF + HO_2$	2.78×10^{-11}	10	SAR
123	$HOOCH_2SCH_2OH \rightarrow OCH_2SCH_2OH + OH$	J("CH3OOH")	10	SAR
124	$HOOCH_2SCH_2OOH + OH \rightarrow HOOCH_2SCH_2O_2$	$2 \times 3.68 \times 10^{-13} \times e^{(635/T)}$	10	SAR
125	$HOOCH_2SCH_2OOH \rightarrow HOOCH_2SCH_2O + OH$	J("CH3OOH")	10	SAR
126	$HOOCH_2SCH_2O_2 + HO_2 \rightarrow HOOCH_2SCH_2OOH$	KRO2HO2 × 0.387	10	SAR
127	$HOOCH_2SCH_2O_2 + NO_3 \rightarrow HOOCH_2SCH_2O + NO_2$	KRO2NO3	10	SAR
128	$HOOCH_2SCH_2O_2 + NO \rightarrow HOOCH_2SCH_2O + NO_2$	$4.9 \times 10^{-12} \times e^{(260/T)}$	10	SAR
129	$HOOCH_2SCH_2O_2 \rightarrow HOOCH_2SCH_2O$	$3.74 \times 10^{-12} \times [RO_2] \times 0.8$	10	SAR
130	$HOOCH_2SCH_2O_2 \rightarrow HOOCH_2SCH_2OH$	$3.74 \times 10^{-12} \times [RO_2] \times 0.1$	10	SAR
131	$HOOCH_2SCH_2O_2 \rightarrow HPMTF$	$3.74 \times 10^{-12} \times [RO_2] \times 0.1$	10	SAR
132	$HOOCH_2SCH_2O_2 \rightarrow HPMTF + OH$	$6.1 \times 10^{11} \times e^{(-9.5 \times 10^3/T + 1.1 \times 10^8/T^3)}$	5	Theory
133	$HOOCH_2SO + NO_2 \rightarrow SO_2 + HCHO + OH + NO$	1.2×10^{-11}	10	SAR
134	$HOOCH_2SO + O_3 \rightarrow SO_2 + HCHO + OH$	4.0×10^{-13}	10	SAR
135	$HOOCH_2SOO \rightarrow HOOCH_2S$	**KRSOOb**	*f*	SAR
136	$HOOCH_2SOO \rightarrow SO_2 + HCHO + OH$	**KRSOOisom**	10	SAR
137	$HOOCH_2SOO \rightarrow TPA + HO_2$	$7.13 \times 10^{-31} \times T^{14.02} \times e^{(-2556/T)}$	5	Theory

138	HPMTF $\rightarrow$ $HOOCH_2S$ + HO_2 + CO	J("C3H7CHO")	10		SAR
139	HPMTF $\rightarrow$ OCH_2SCHO + OH	J("CH3OOH")	10		SAR
140	HPMTF + OH $\rightarrow$ $HOOCH_2S$ + CO	$1.75 \times 10^{-11} \times 0.91$	3		Indirect
141	HPMTF + OH $\rightarrow$ OH + HCHO + OCS	$1.75 \times 10^{-11} \times 0.09$	3		Indirect
142	HSO_3 $\rightarrow$ HO_2 + SO_3	$1.3 \times 10^{-12} \times e^{(-330/T)} \times [O_2]$	1.32	200	Evaluated
143	MSA + OH $\rightarrow$ CH_3SO_3	2.24×10^{-14}	10		SAR
144	MSIA + NO_3 $\rightarrow$ CH_3SO_2 + HNO_3	1.00×10^{-13}	10		Estimate
145	MSIA + OH $\rightarrow$ CH_3SO_2	9.00×10^{-11}	1.96		Evaluated
146	MSIA + O_3 $\rightarrow$ MSA	1.79×10^{-22}	5		Theory
147	OCHSCHO + OH $\rightarrow$ OCS + CO + HO_2	2.6×10^{-11}	5		Theory
148	OCHSCHO $\rightarrow$ OCS + HO_2 + CO + HO_2	J("C3H7CHO")	10		SAR
149	OCHSOH + OH $\rightarrow$ OCS + OH	1.40×10^{-12}	5		Theory
150	OCHSOH $\rightarrow$ CO + HO_2 + SO + HO_2	J("C3H7CHO")	10		SAR
151	OCH_2SCHO $\rightarrow$ HCHO + OCS + HO_2	KDEC	10		SAR
152	OCH_2SCH_2OH $\rightarrow$ $HOCH_2S$ + HCHO	KDEC	10		SAR
153	OCS + O $\rightarrow$ CO + SO	$2.1 \times 10^{-11} \times e^{(-2200/T)}$	1.32	150	Evaluated
154	OCS + OH $\rightarrow$ SO + OH	$7.2 \times 10^{-14} \times e^{(-1070/T)}$	2	200	Evaluated
155	SO + NO_2 $\rightarrow$ SO_2 + NO	1.40×10^{-11}	1.44	50	Evaluated
156	SO + O_3 $\rightarrow$ SO_2	$3.4 \times 10^{-12} \times e^{(-1100/T)}$	1.21	150	Evaluated
157	SO + OH $\rightarrow$ SO_2 + HO_2	$2.6 \times 10^{-11} \times e^{(330/T)}$	1.32	150	Evaluated
158	SO $\rightarrow$ SO_2 + O	$1.6 \times 10^{-13} \times e^{(-2280/T)} \times [O_2]$	1.44	200	Evaluated
159	**SO + BrO $\rightarrow$ SO_2**	$\mathbf{5.7 \times 10^{-11}}$	1.96		Evaluated[1]
160	SO_2 + OH $\rightarrow$ HSO_3	KTER2	3	100	Evaluated
161	SO_2 + O $\rightarrow$ SO_3	KTER	2	100	Evaluated
162	SO_3 + NO_2 $\rightarrow$ NSO5	1.00×10^{-19}	10		Evaluated
163	SO_3 $\rightarrow$ SA	$8.5 \times 10^{-41} \times e^{(6540/T)} \times [H_2O]^2$	1.44	200	Evaluated
164	TPA $\rightarrow$ OCS + HO_2 + OH	J("CH3OOH")	10		SAR
165	TPA + OH $\rightarrow$ OCHSOH + OH	$5 \times 10^{-11} \times 0.86$	5		Theory
166	TPA + OH $\rightarrow$ OCS + OH	$5 \times 10^{-11} \times 0.14$	5		Theory

[a] $f^2(T)$ = f^2(298 K)×(e$^{g(1/T-1/298)}$)^2

[b] This reaction has been evaluated by IUPAC (Atkinson et al., 2004), but not the NASA panel report (Burkholder et al., 2019).

[c] Although the self-reaction has been evaluated, the lumped RO_2 rate constant involves structure activity relationships for branching ratios

[d] Estimate from this work based on experimental upper limit (Urbanski and Wine, 1999; Berndt, 2025)

[e] Total reaction has been evaluated by the NASA panel report, however the branching ratios are from Borissenko et al. (2003).

[f] This reaction is an equilibrium reaction where the uncertainty was only included for the forward reaction, based on the uncertainty in the equilibrium rate constant

References: [1] Burkholder et al. (2019), [2] Enami et al. (2004), [3] Aranda et al. (2002), [4] Chen et al. (2023),[5] Berndt (2025)

Rate constants: KRSOOb = $1.20\times10^{-16}\times$e$^{1580/T}/(1.4\times10^{-26}\times$e$^{4850/T})$, KRSOO2b = $3.12\times10^{-16}\times$e$^{1580/T}/(2.35\times10^{-18}\times6.76\times10^{-10}\times$e$^{3.48\times10^{-3}T})$, KRSO2O2b = $1.03\times10^{-16}\times$e$^{1580/T}/(2.35\times10^{-18}\times5.76\times10^{13}\times$e$^{-8.86\times10^{-2}T})$, KRSOOisom = $7\times10^{14}\times$e$^{-9659/T}$, KDMSOH = [M]$\times3\times10^{-31}(T/298)^{-6.24}/(9.6\times10^{-27}\times$e$^{5376/T})$, KTER = (KinfT ×K0T×[M])×(0.6$^{\text{Kb}}$)/(KinfT+K0T×[M]), KinfT = $4.1\times10^{-14}\times(T/298)^{1.8}$, K0T = $1.8\times10^{-33}\times(T/298)^2$, Kb = $(1+(\log_{10}(\text{K0T}\times[\text{M}]/\text{KinfT}))^2)^{-1}$, KTER2 = (KinfT2 ×K0T2×[M])×(0.6$^{\text{Kb2}}$)/(KinfT2+K0T2×[M]), KinfT2 = $1.7\times10^{-12}\times(T/298)^{0.2}$, K0T2 = $2.9\times10^{-31}\times(T/298)^{-4.1}$, Kb2 = $(1+(\log_{10}(\text{K0T2}\times[\text{M}]/\text{KinfT2}))^2)^{-1}$, KRO2HO2 = $2.91\times10^{-13}\times$e$^{1300/T}$, KRO2NO3 = 2.3×10^{-12}, J("CH3OOH") = photolysis rate for CH_3OOH, KDEC = 1.0×10^6, J("C3H7CHO") = photolysis rate for n-C_3H_7CHO forming a HCO radical, KRO2NO = $2.7\times10^{-12}\times$e$^{360/T}$, KAPHO2 = $5.2\times10^{-13}\times$e$^{980/T}$

S5 Comparisons of the original, updated and expanded dimethyl sulfide mechanisms

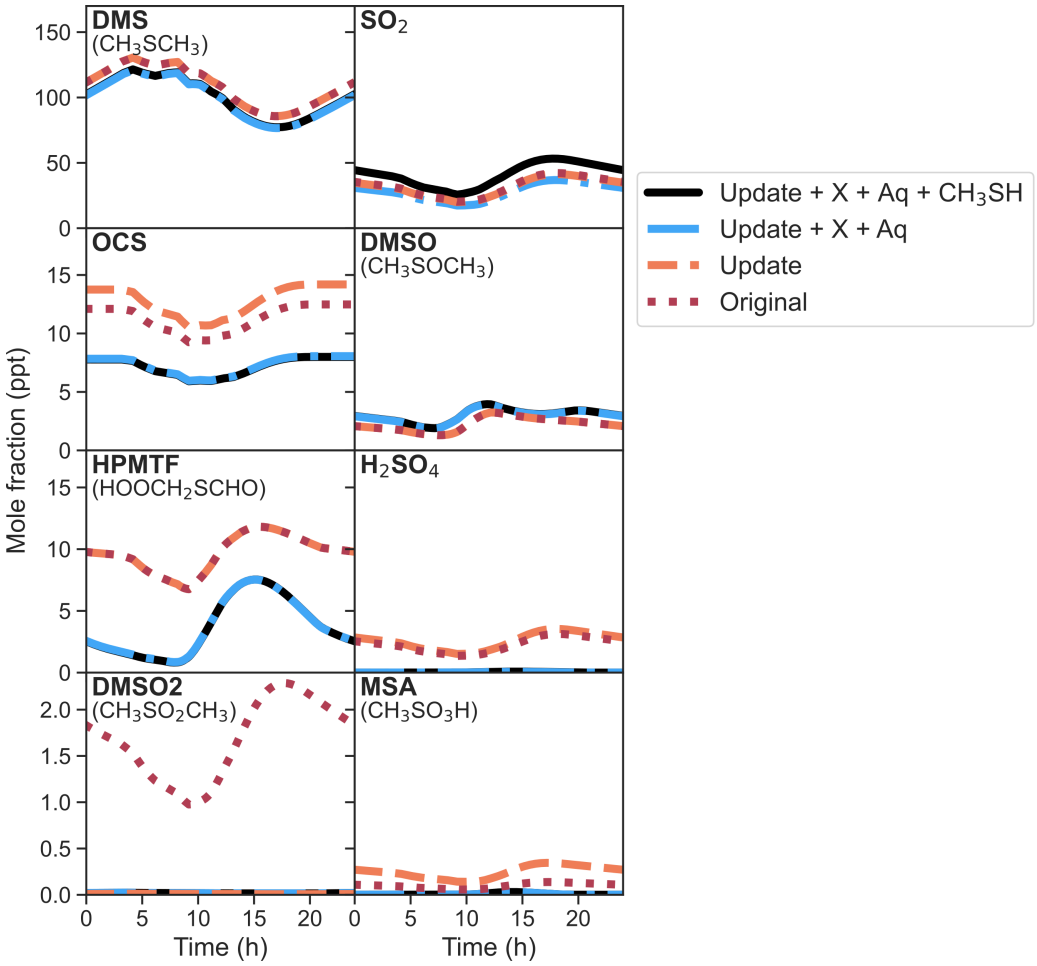

Figure S7. Mixing ratios of DMS, SO_2, OCS, DMSO, HPMTF, H_2SO_4, DMSO2 and MSA from the Cape Grim (temperate) box model, using the original mechanism from Jacob et al. (2024) (Original, red dotted line), the updated gas-phase OH-initiated DMS oxidation mechanism (Update, orange dashed line), the updated mechanism with the addition of BrO, Cl atoms, aerosol uptake and aqueous chemistry (Update + X + Aq, blue dot-dashed line) and the mechanism used in this work, including CH_3SH chemistry (Update + X + Aq + CH_3SH, black line).

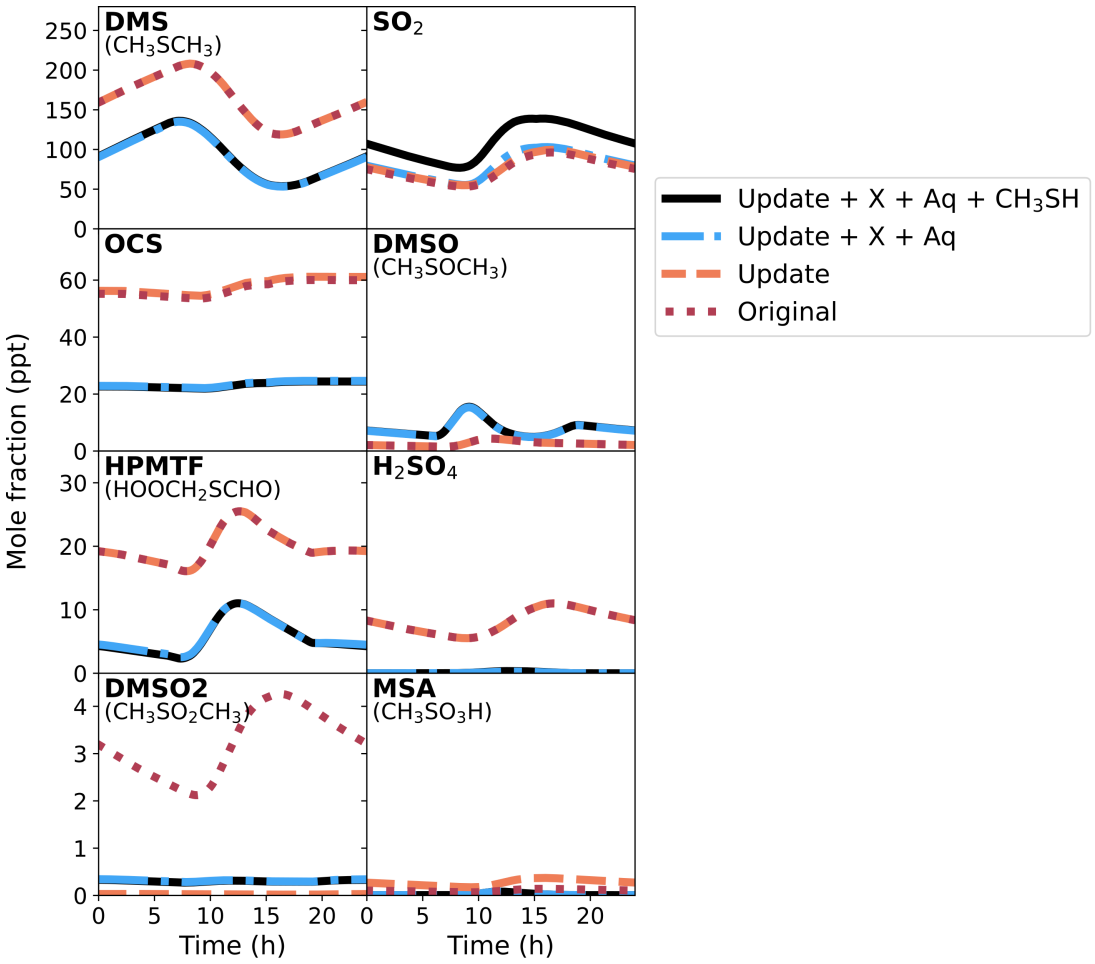

Figure S8. Mixing ratios of DMS, SO_2, OCS, DMSO, HPMTF, H_2SO_4, DMSO2 and MSA from the Cape Verde (tropical) box model, using the original mechanism from Jacob et al. (2024) (Original, red dotted line), the updated gas-phase OH-initiated DMS oxidation mechanism (Update, orange dashed line), the updated mechanism with the addition of BrO, Cl atoms, aerosol uptake and aqueous chemistry (Update + X + Aq, blue dot-dashed line) and the mechanism used in this work, including CH_3SH chemistry (Update + X + Aq + CH_3SH, black line).

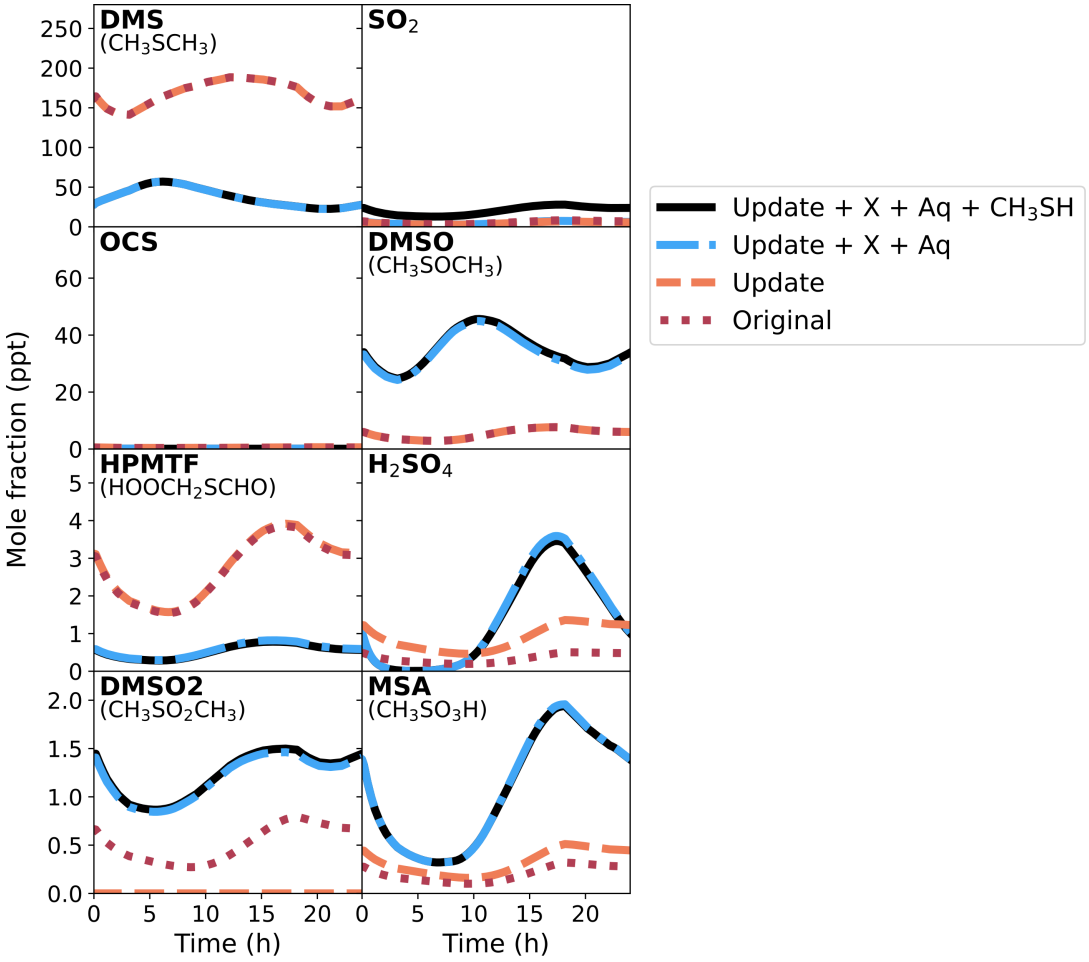

Figure S9. Mixing ratios of DMS, SO_2, OCS, DMSO, HPMTF, H_2SO_4, DMSO2 and MSA from the Halley Station (polar) box model, using the original mechanism from Jacob et al. (2024) (Original, red dotted line), the updated gas-phase OH-initiated DMS oxidation mechanism (Update, orange dashed line), the updated mechanism with the addition of BrO, Cl atoms, aerosol uptake and aqueous chemistry (Update + X + Aq, blue dot-dashed line) and the mechanism used in this work, including CH_3SH chemistry (Update + X + Aq + CH_3SH, black line).

S6 Meteorological conditions and gas-phase concentrations

The Reactive Halogen in the Marine Boundary Layer (RHaMBLe) project took place at the Cape Verde Atmospheric Observatory (CVAO, 16.86°N, 24.87°W) in May and June 2007 (Lee et al., 2010). The station is located on a beach that faces consistent NE winds, to sample marine air that is generally free from local pollution. On May 15th-20th, back trajectories identified that the station was specifically sampling air from the remote North Atlantic Ocean that had passed close to the Canary Islands (Lee et al., 2010). The data from these days were chosen to constrain the tropical climate box model (Natural Environment Research Council et al., 2006).

The Southern Ocean Atmospheric Photochemistry Experiment 2 (SOAPEX2) was conducted at Cape Grim, Australia (40.68°S, 144.69°E) in January and February 1999 (Sommariva et al., 2004). The experiments were based at the Cape Grim Baseline Atmospheric Pollution Station (CGBAPS), which is situated 100 m above sea level (on a cliff-top) and 100 m inland. Depending on the meteorological conditions, the station can sample clean air that is representative of the Southern Ocean. During the campaign, four days (Feb 7th-8th, and Feb 15th-16th) were classified as sampling this 'baseline air' due to the low concentrations of NO_x and non-methane hydrocarbons measured (Sommariva et al., 2004). The concentrations of oxidants and DMS on those days were used to constrain the temperate climate box model run (Allan et al., 1987). BrO was not measured in the Cape Grim campaign; modelled BrO was based on ATom measurements over the marine environment below 2 km in altitude, which measured an average mixing ratio of 0.1 ppt Veres et al. (2020).

Chemistry of the Antarctic Boundary Layer and the Interface with Snow (CHABLIS) was a campaign conducted at Halley Research Station, Antarctica (75.58°S, 26.65°W) from February 2004 to February 2005 (Jones et al., 2008; Natural Environment Research Council et al., 2005). Halley Station is located 32 m above sea level and 15 km inland; the measurements were conducted in the Clean Air Sector Laboratory, which is located 1 km southeast of the main station, to minimise the effects of local pollution. Measurements of OH and HO_2 were performed in January and February 2005 (Bloss et al., 2007), and the 29th of January was identified as having an air mass originating from the Weddell Sea (Saiz-Lopez et al., 2007). Where possible, data from that day was chosen to constrain the polar climate box model; this data includes DMS (Read et al., 2008), OH and HO_2 (Bloss et al., 2007), $HCHO$ (Salmon et al., 2008), O_3 (Jones et al., 2008), NO_x (Bauguitte et al., 2012), CO (Jones et al., 2008) and relative humidity and temperature (Natural Environment Research Council et al., 2005). A peak BrO mixing ratio of 6 ppt was chosen based on the BrO measured on the 1st December 2004 (Saiz-Lopez et al., 2007), representing a summer day with an air mass from the Weddell Sea.

ECMWF Reanalysis v5 (ERA5) data was used to supplement the fieldwork data and provide additional input parameters, such as the friction velocity and 10 metre u and v wind components, which are required to calculate the deposition velocity, along with boundary layer height (Hersbach et al., 2023). In each case, the ERA5 coordinates over the ocean that were closest to the fieldwork data were chosen, specifically: 17.00°N, 24.75°W for Cape Verde, 40.75°S and 144.50°E for Cape Grim, and 75.25°S and 26.75°W for Halley Station. The deposition velocity was calculated through a resistance method, which is described in Section S6.1. Additionally, ERA5 data was used to provide relative humidity, temperature and pressure data for the Cape Grim box model, as those fieldwork measurements were not accessible.

S6.1 Dry deposition

The dry deposition scheme was based off the resistance scheme from Hicks et al. (1987), with the total deposition velocity, V_{d}, a combination of three resistance variables, R_{a}, R_{b}, and R_{c}, corresponding to aerodynamic resistance, diffusive boundary resistance and surface resistance, respectively,

$$V_{\mathrm{d}} = \frac{1}{R_{\mathrm{a}} + R_{\mathrm{b}} + R_{\mathrm{c}}}$$

For the dry deposition of trace gases, R_{a} and R_{c} tend to dictate the dry deposition velocity (Hicks et al., 1987).

An approximation for aerodynamic resistance (R_{a}) is used, which is based on wind speed (calculated from the u and v-component 10 meter velocity in m s^{-1}, u_{10} and v_{10}, respectively) and frictional velocity, u_{s} (m s^{-1}),

$$R_{\mathrm{a}} \approx \sqrt{(u_{10}^2 + v_{10}^2)} u_{\mathrm{s}}^{-2}$$

The resistance due to diffusion of a gas, X, into the immediate vicinity of the surface, R_{b}, is given by

$$R_{\mathrm{b}} = \frac{2}{\kappa u_{\mathrm{s}}} (\frac{\mathrm{Sc}}{\mathrm{Pr}})^{\mathrm{p}}$$

where Pr is the Prandtl number for air (Pr ≈ 0.72), κ is the von Karman constant (0.4), p is a constant often taken to be $\frac{2}{3}$ and Sc is the Schmidt number for species X,

$$\mathrm{Sc} = \frac{v_{\mathrm{air}}}{D_{\mathrm{g}}}$$

with v_{air} the viscosity of air (m^2 s^{-1}) and D_{g} the gas-phase diffusion of species X (m^2 s^{-1}). The D_{g} used in this work is given in Table S1.

Finally, the surface resistance for a compound, R_{c}, is dependent on the surface type; as all the box models in this work are above the ocean, only water surface resistance needs to be considered. An R_{c} of 20 s m^{-1} was used for $\mathrm{SO_2}$, based on Zhang et al. (2003). For $\mathrm{O_3}$, a resistance of 2000 s m^{-1} was used, based on Wesely (1989). The DMS oxidation species that have Henry's law coefficients a factor of 1000 higher than $\mathrm{SO_2}$ (DMSO, DMSO2, MSA, MSIA, $\mathrm{H_2SO_4}$, TPA and HPMTF, from Table S1) were given an R_{c} value of 1 s m^{-1}, as these higher Henry's law coefficients indicate that these species are highly water soluble.

S7 Aerosol measurements

Aerosol composition measurements taken during both the Halley Station CHABLIS campaign (Read et al., 2008), and the Cape Verde RHaMBLe campaign (Sander et al., 2013; Müller et al., 2010; Fomba et al., 2014), were used to derive aerosol liquid water content (LWC) and pH. The measurements from Read et al. (2008) from the CHABLIS campaign were used for the Halley Station model. For the Cape Verde model, the year-long average of Na^+ and Cl^- from Fomba et al. (2014) was used (2007-2011), as the authors showed that sea salt concentrations were consistent throughout the year and mostly fluctuated with wind speed. Additionally, the average concentration of $NO_3{}^-$ and $NH_4{}^+$ in May 2007 measured by Fomba et al. was utilised, along with the concentration of MSA and non-sea salt SO_4^{2-} from May 15th-20th from Müller et al. (2010) measurements. The total SO_4^{2-} concentration was back-calculated from the concentration of Na^+ ($[SO_4^{2-}]$=$[Na^+]\times$0.2517, (Millero, 2013)). No aerosol measurements were taken during the Cape Grim SOAPEX2 campaign; however, aerosol concentration measurements were taken at Cape Grim from November 1988 - August 1990 (Andreae et al., 1999). The concentrations of the ions measured, including the average measurements at Cape Grim in February 1989 and 1990, are included in Table 1 of the main text. These concentrations, along with the average temperature, were used as inputs into the Extended Aerosol Inorganics Model (E-AIM) IV (Wexler, 2002; Clegg et al., 1998, 1992) to obtain aerosol LWC and pH as a function of relative humidity (RH) shown in Figure S11. However, the resulting RH-dependence of LWC assumes an initially solid aerosol with increasing RH that undergoes deliquescence (becoming a liquid aerosol) once a critical RH is reached (74% for Cape Grim and 72% for Cape Verde). An aerosol that is initially liquid with decreasing RH will become solid at a much lower RH (around 41-51% for a NaCl-based aerosol, according to Peng et al. (2022)). In order to model liquid aerosols representative of the marine environment, at relative humidities below the deliquescence relative humidity E-AIM III modelling results with NaCl crystallisation turned off were used instead (E-AIM IV does not allow NaCl crystallisation to be turned off). This combined E-AIM modelled data was used, along with time-dependent relative humidity from either ERA5 data (in the case of Cape Grim) or the campaign measurements, to obtain liquid water content and pH over the modelled day, which is given in Figure S10.

The aqueous concentration of ozone was found using the same method as Chen et al. (2018), where gas-liquid equilibrium was assumed using Henry's Law. The reactions with ozone in the aqueous-phase did not affect the concentrations in our modelling.

The OH aqueous concentration in marine aerosols has been indirectly measured and ranges from 5×10^{-16}-1×10^{-15} M, with marine cloud droplets measuring 9×10^{-16} M (Arakaki et al., 2013). In our modelling, the OH aqueous concentration was constrained to a constant concentration of 8×10^{-16} M, based on an average of the measured aerosol measurements.

To calculate the rate of adsorption into an aerosol for different species in our model, in addition to temperature and aerosol liquid water content, the aerosol radius is required. In the SPACCIM model, a well-mixed deliquesced aerosol containing insoluble and soluble compounds is assumed, however, the Schwartz approach used in this work and the SPACCIM model also assumes a well-diluted droplet (Wolke et al., 2005). Following personal correspondence with Eric Hoffmann, it was identified that the aerosol modelling used in Hoffmann et al. (2016) divided the aerosol radius (0.38 μm) by 10 to create a 'pseudo water particle' with a radius of 0.038 μm.

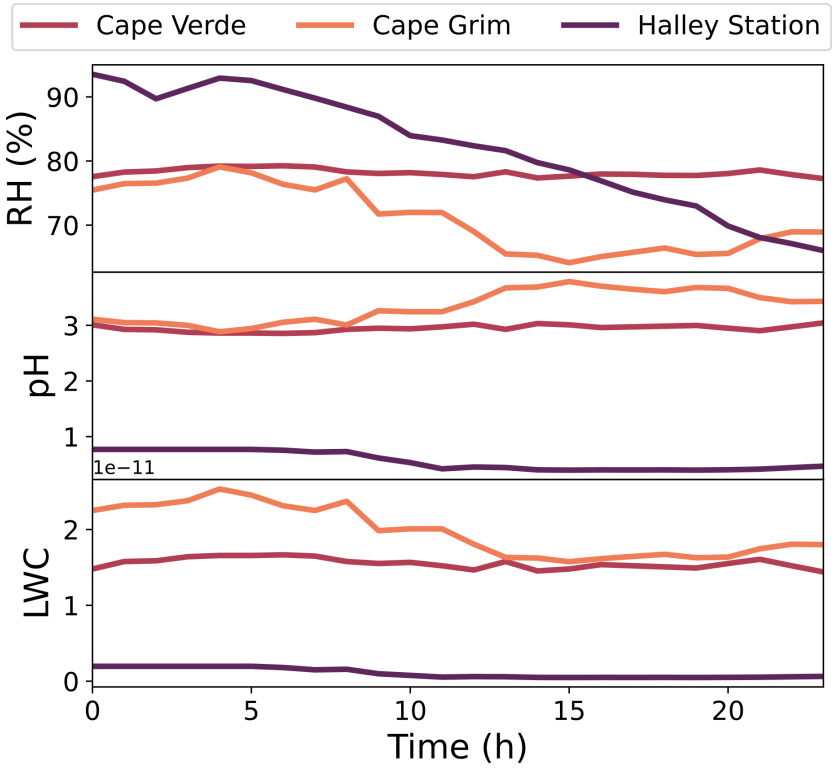

Figure S10. The relative humidity (RH) used in the calculations, along with the calculated aerosol pH and the unitless liquid water content (LWC, w/w) for the Cape Verde, Cape Grim, and Halley Station box models.

To evaluate the calculated absorption rate (along with the aerosol radius used), the absorption rate of sulfuric acid (H_2SO_4) can be directly compared to observed condensation sinks. (Ranjithkumar et al., 2021) used data from four Atmospheric Tomography (ATom) field campaigns (ATom1-4) and separated them by latitude bands, which included tropics (25°N-25°S), lower midlatitudes (25-60°S) and lower high latitudes (60°S-90°S) (Wofsy et al.). Figure S12 shows the interquartile range (25th-75th percentile) of the measured condensation sink in the lowest altitude bin (0.18-1 km) in the three latitude bands. The adsorption rate calculated from the radius of the 'pseudo water particle' used by Hoffmann et al. (and the aerosol liquid water content and temperature for each model described above) is up to a factor of 50 higher than the observed condensation sink for the southern midlatitudes, and a factor of 10 for both the tropics and southern high-latitudes (Figure S12). Using the same aerosol radius as the Hoffmann et al. model (0.38 µm) without a correction factor results in a maximum calculated condensation sink within a factor of two of the observed values and, as such, was used for this work.

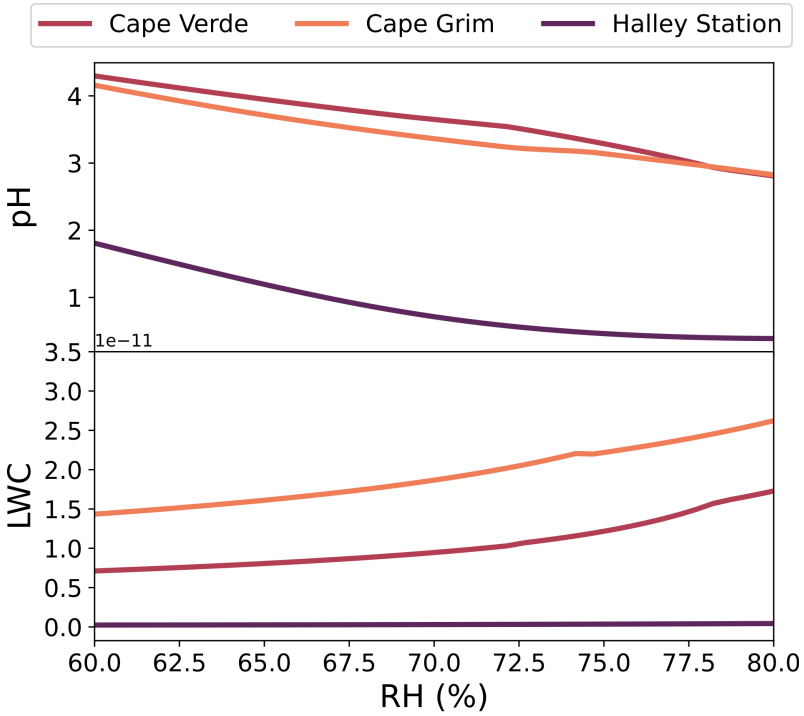

Figure S11. The relative humidity (RH) dependence of aerosol pH and unitless liquid water content (LWC, w/w) calculated for the Cape Verde, Cape Grim and Halley Station box models.

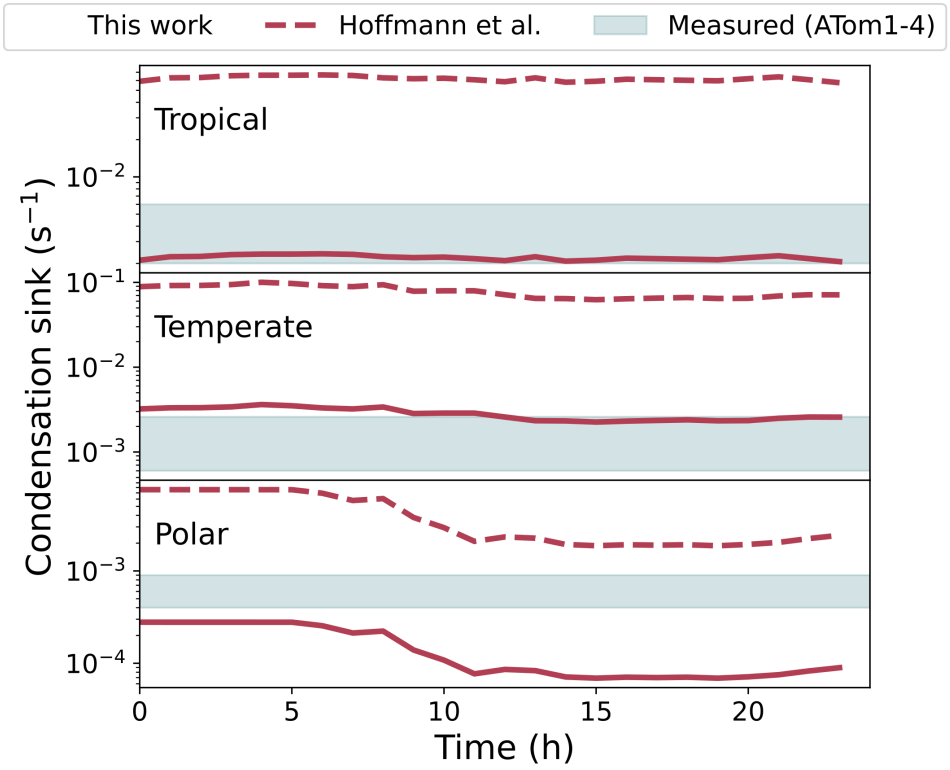

Figure S12. The condensation sink (adsorption rate of sulfuric acid onto aerosol) calculated in this work (solid line) for the Cape Verde, Cape Grim and Halley Station models (labelled tropical, temperate and polar, respectively), compared to the condensation sink calculated using the factor of 10 correction to aerosol radius used by Hoffmann et al. (2016) (dashed line). The grey bar represents the interquartile range of observed condensation sinks by ATom flight campaigns 1-4 from 0.18-1 km altitude in tropical, southern midlatitudes and southern high-latitude bands (referred to here as tropical, temperate and polar, respectively) (Ranjithkumar et al., 2021; Wofsy et al.).

S8 Input parameters for the three marine box models

Table S3. The additional loss rates for OH and HO_2 (s^{-1}) used in the Cape Verde, Cape Grim and Halley Station box models.

	Cape Verde	Cape Grim	Halley Station
OH	0.4	0.08	0
HO_2	0.02	0.004	0.01

Table S4. The initial mixing ratios (ppm) used in the Cape Verde, Cape Grim and Halley Station box models.

	Cape Verde	Cape Grim	Halley Station
H_2O	21288	14944	3190
H_2	0.5	0.5	0.5
H_2O_2	0.001	0.001	0.001
NO	3.00×10^{-6}	1.00×10^{-6}	7.00×10^{-7}
NO_2	3.00×10^{-5}	1.00×10^{-5}	7.00×10^{-6}
HNO_3	1.50×10^{-3}	5.00×10^{-4}	2.50×10^{-4}
O_3	0.035	0.016	0.01
CH_4	1.8	1.688	1.8
CO	0.104	0.041	0.035
DMS	1.00×10^{-4}	1.00×10^{-4}	4.00×10^{-5}
SO_2	2.00×10^{-5}	2.00×10^{-5}	2.00×10^{-5}
CH_3SH	2.00×10^{-5}	8.00×10^{-6}	1.20×10^{-5}
HCHO	3.28×10^{-4}	0	1.50×10^{-4}

Table S5. The emissions (molecules cm^{-2} s^{-1}) used in the Cape Verde, Cape Grim and Halley Station box models.

	Cape Verde	Cape Grim	Halley Station
DMS	3.50×10^{9}	3.80×10^{9}	4.00×10^{9}
O_3	1.20×10^{11}	4.60×10^{10}	1.00×10^{10}
CH_3SH	7.70×10^{8}	6.84×10^{8}	1.20×10^{9}
CO	2.00×10^{10}	0	0
HCHO	0	1.20×10^{10}	2.50×10^{9}

Table S6. The deposition velocities (cm s^{-1}) over the diurnal cycle used in the Cape Verde model.

Time (h)	SO_2	O_3	MSA	MSIA	DMSO	DMSO2	H_2SO_4	HPMTF	TPA
0	0.77	0.05	0.87	0.90	0.89	0.89	0.89	0.89	0.90
1	0.77	0.05	0.86	0.89	0.88	0.88	0.88	0.87	0.89
2	0.76	0.05	0.86	0.88	0.87	0.87	0.87	0.87	0.88
3	0.75	0.05	0.84	0.86	0.86	0.85	0.86	0.85	0.86
4	0.72	0.05	0.80	0.83	0.82	0.82	0.82	0.82	0.83
5	0.71	0.05	0.79	0.81	0.81	0.80	0.81	0.80	0.82
6	0.73	0.05	0.81	0.83	0.83	0.82	0.83	0.82	0.84
7	0.81	0.05	0.92	0.94	0.93	0.93	0.93	0.93	0.94
8	0.83	0.05	0.95	0.97	0.97	0.96	0.97	0.96	0.98
9	0.85	0.05	0.97	1.00	0.99	0.98	0.99	0.98	1.00
10	0.85	0.05	0.98	1.01	1.00	1.00	1.00	0.99	1.01
11	0.84	0.05	0.96	0.99	0.98	0.98	0.98	0.97	0.99
12	0.82	0.05	0.93	0.96	0.95	0.95	0.95	0.94	0.96
13	0.80	0.05	0.90	0.93	0.92	0.92	0.92	0.92	0.93
14	0.79	0.05	0.89	0.91	0.91	0.90	0.91	0.90	0.92
15	0.76	0.05	0.85	0.87	0.87	0.86	0.87	0.86	0.88
16	0.73	0.05	0.81	0.84	0.83	0.83	0.83	0.83	0.84
17	0.71	0.05	0.80	0.82	0.81	0.81	0.81	0.81	0.82
18	0.72	0.05	0.81	0.83	0.82	0.82	0.82	0.82	0.83
19	0.79	0.05	0.90	0.92	0.92	0.91	0.92	0.91	0.93
20	0.80	0.05	0.91	0.94	0.93	0.92	0.93	0.92	0.94
21	0.79	0.05	0.89	0.92	0.91	0.90	0.91	0.90	0.92
22	0.77	0.05	0.87	0.89	0.89	0.88	0.89	0.88	0.90
23	0.76	0.05	0.86	0.88	0.87	0.87	0.87	0.87	0.88

Table S7. The deposition velocities (cm s^{-1}) over the diurnal cycle used in the Cape Grim model.

Time (h)	SO_2	O_3	MSA	MSIA	DMSO	DMSO2	H_2SO_4	HPMTF	TPA
0	1.00	0.05	1.19	1.19	1.22	0.76	1.21	1.17	1.21
1	0.92	0.05	1.08	1.08	1.11	0.72	1.10	1.07	1.10
2	0.86	0.05	0.99	0.99	1.01	0.68	1.01	0.98	1.01
3	0.96	0.05	1.13	1.13	1.15	0.74	1.15	1.11	1.15
4	1.11	0.05	1.35	1.35	1.39	0.83	1.38	1.33	1.38
5	1.25	0.05	1.57	1.57	1.62	0.90	1.61	1.55	1.61
6	0.97	0.05	1.15	1.15	1.18	0.75	1.17	1.13	1.17
7	1.02	0.05	1.21	1.21	1.25	0.77	1.24	1.20	1.24
8	1.12	0.05	1.37	1.37	1.41	0.83	1.40	1.35	1.40
9	1.26	0.05	1.58	1.58	1.63	0.91	1.61	1.56	1.61
10	1.31	0.05	1.68	1.68	1.73	0.94	1.71	1.65	1.71
11	1.29	0.05	1.64	1.64	1.69	0.92	1.67	1.62	1.67
12	1.29	0.05	1.64	1.64	1.69	0.92	1.68	1.62	1.68
13	1.29	0.05	1.64	1.64	1.69	0.92	1.67	1.62	1.67
14	1.29	0.05	1.65	1.65	1.70	0.93	1.68	1.63	1.68
15	1.31	0.05	1.67	1.67	1.72	0.93	1.71	1.65	1.71
16	1.31	0.05	1.67	1.67	1.72	0.93	1.71	1.65	1.71
17	1.29	0.05	1.65	1.65	1.70	0.93	1.68	1.63	1.68
18	1.24	0.05	1.56	1.56	1.60	0.90	1.59	1.54	1.59
19	1.17	0.05	1.45	1.45	1.49	0.86	1.48	1.43	1.48
20	1.11	0.05	1.35	1.35	1.39	0.83	1.37	1.33	1.37
21	1.08	0.05	1.31	1.31	1.35	0.81	1.34	1.29	1.34
22	1.06	0.05	1.27	1.27	1.31	0.80	1.30	1.25	1.30
23	1.04	0.05	1.25	1.25	1.29	0.79	1.27	1.23	1.27

Table S8. The deposition velocities (cm s^{-1}) over the diurnal cycle used in the Halley Station model.

Time (h)	SO_2	O_3	MSA	MSIA	DMSO	DMSO2	H_2SO_4	HPMTF	TPA
0	0.39	0.04	0.40	0.41	0.41	0.41	0.41	0.41	0.41
1	0.49	0.05	0.53	0.54	0.54	0.53	0.54	0.53	0.54
2	0.60	0.05	0.66	0.68	0.67	0.67	0.67	0.67	0.68
3	0.72	0.05	0.81	0.83	0.82	0.82	0.82	0.82	0.83
4	0.86	0.05	0.99	1.02	1.01	1.01	1.01	1.01	1.02
5	0.97	0.05	1.14	1.18	1.17	1.16	1.17	1.16	1.18
6	1.06	0.05	1.27	1.30	1.29	1.29	1.29	1.28	1.31
7	1.15	0.05	1.41	1.46	1.44	1.44	1.44	1.43	1.46
8	1.27	0.05	1.60	1.65	1.64	1.63	1.63	1.62	1.66
9	1.35	0.05	1.74	1.79	1.78	1.77	1.77	1.76	1.80
10	1.40	0.05	1.83	1.89	1.87	1.86	1.87	1.86	1.90
11	1.42	0.05	1.86	1.92	1.91	1.90	1.90	1.89	1.93
12	1.39	0.05	1.81	1.87	1.86	1.85	1.85	1.84	1.88
13	1.38	0.05	1.79	1.85	1.83	1.82	1.83	1.82	1.86
14	1.39	0.05	1.80	1.86	1.85	1.84	1.85	1.83	1.87
15	1.39	0.05	1.80	1.86	1.84	1.83	1.84	1.83	1.87
16	1.34	0.05	1.72	1.78	1.76	1.75	1.76	1.75	1.78
17	1.27	0.05	1.61	1.66	1.64	1.63	1.64	1.63	1.66
18	1.17	0.05	1.43	1.48	1.47	1.46	1.47	1.46	1.48
19	1.07	0.05	1.28	1.32	1.31	1.31	1.31	1.30	1.33
20	0.97	0.05	1.14	1.18	1.17	1.16	1.16	1.16	1.18
21	0.87	0.05	1.00	1.03	1.02	1.02	1.02	1.01	1.03
22	0.70	0.05	0.78	0.80	0.80	0.79	0.80	0.79	0.81
23	0.52	0.05	0.56	0.57	0.57	0.57	0.57	0.57	0.57

Table S9. The temperature, planetary boundary layer (PBL) height, pressure, BrO mixing ratio, Cl atom concentration, aerosol liquid water content (LWC), and aerosol pH over the diurnal cycle used in the Cape Verde model.

Time (h)	Temperature (K)	PBL height (m)	Pressure (atm)	BrO (ppt)	Cl (molec cm^{-3})	LWC	pH
0	295.8	673	1.00	0.00	0	1.48×10^{-11}	3.01
1	295.8	666	1.00	0.00	0	1.58×10^{-11}	2.93
2	295.7	664	1.00	0.00	0	1.59×10^{-11}	2.92
3	295.5	668	1.00	0.00	0	1.64×10^{-11}	2.88
4	295.5	670	1.00	0.00	0	1.66×10^{-11}	2.86
5	295.4	673	1.00	0.00	0	1.66×10^{-11}	2.86
6	295.6	676	1.00	0.00	0	1.67×10^{-11}	2.86
7	295.5	680	1.00	1.22	106	1.65×10^{-11}	2.87
8	295.6	686	1.00	1.94	1626	1.58×10^{-11}	2.93
9	295.8	694	1.00	2.33	4748	1.55×10^{-11}	2.95
10	295.9	699	1.00	2.57	8497	1.57×10^{-11}	2.94
11	295.8	702	1.00	2.72	11811	1.52×10^{-11}	2.97
12	296.1	713	1.00	2.79	13817	1.47×10^{-11}	3.02
13	296.2	724	1.00	2.80	14004	1.58×10^{-11}	2.93
14	296.1	744	1.00	2.74	12327	1.45×10^{-11}	3.03
15	296.1	764	1.00	2.61	9210	1.48×10^{-11}	3.01
16	296.2	768	1.00	2.39	5467	1.54×10^{-11}	2.96
17	296.0	772	1.00	2.03	2138	1.52×10^{-11}	2.97
18	296.1	763	1.00	1.41	250	1.51×10^{-11}	2.99
19	296.0	757	1.00	0.00	0	1.49×10^{-11}	3.00
20	295.9	756	1.00	0.00	0	1.55×10^{-11}	2.95
21	295.9	757	1.00	0.00	0	1.61×10^{-11}	2.90
22	295.9	751	1.00	0.00	0	1.52×10^{-11}	2.97
23	295.8	738	1.00	0.00	0	1.44×10^{-11}	3.04

Table S10. The temperature, planetary boundary layer (PBL) height, pressure, BrO mixing ratio, Cl atom concentration, aerosol liquid water content (LWC), and aerosol pH over the diurnal cycle used in the Cape Grim model.

Time (h)	Temperature (K)	PBL height (m)	Pressure (atm)	BrO (ppt)	Cl (molec cm^{-3})	LWC	pH
0	288.1	1059	1.00	0.00	0	2.25×10^{-11}	3.11
1	288.2	1041	1.00	0.00	0	2.32×10^{-11}	3.05
2	288.3	1010	1.00	0.00	0	2.33×10^{-11}	3.04
3	288.2	988	1.00	0.00	0	2.38×10^{-11}	3.00
4	288.0	1004	0.99	0.00	0	2.53×10^{-11}	2.88
5	288.0	1071	1.00	0.00	0	2.45×10^{-11}	2.94
6	287.9	1133	1.00	0.00	0	2.31×10^{-11}	3.06
7	288.0	1159	1.00	0.02	0	2.25×10^{-11}	3.11
8	288.0	1189	1.00	0.12	91	2.37×10^{-11}	3.01
9	288.9	1303	1.00	0.17	593	1.99×10^{-11}	3.26
10	289.0	1285	1.00	0.20	1452	2.01×10^{-11}	3.25
11	288.8	1323	1.00	0.21	2436	2.01×10^{-11}	3.25
12	289.2	1327	1.00	0.22	3288	1.81×10^{-11}	3.43
13	289.6	1373	1.00	0.23	3797	1.63×10^{-11}	3.67
14	289.7	1385	1.00	0.23	3841	1.62×10^{-11}	3.69
15	289.9	1382	1.00	0.23	3408	1.57×10^{-11}	3.79
16	289.8	1362	1.00	0.22	2602	1.62×10^{-11}	3.70
17	289.7	1313	1.00	0.20	1624	1.65×10^{-11}	3.65
18	289.6	1301	1.00	0.17	723	1.67×10^{-11}	3.61
19	289.6	1228	1.00	0.13	145	1.63×10^{-11}	3.68
20	289.7	1212	1.00	0.05	0	1.64×10^{-11}	3.67
21	288.7	1148	1.00	0.00	0	1.75×10^{-11}	3.50
22	288.6	1092	1.00	0.00	0	1.81×10^{-11}	3.43
23	288.7	1059	1.00	0.00	0	1.80×10^{-11}	3.43

Table S11. The temperature, planetary boundary layer (PBL) height, pressure, BrO mixing ratio, Cl atom concentration, aerosol liquid water content (LWC), and aerosol pH over the diurnal cycle used in the Halley Station model.

Time (h)	Temperature (K)	PBL height (m)	Pressure (atm)	BrO (ppt)	Cl (molec cm^{-3})	LWC	pH
0	271.3	358	0.96	1.76	1	1.97×10^{-12}	0.77
1	271.0	430	0.96	1.20	0	1.97×10^{-12}	0.77
2	270.5	488	0.96	0.99	0	1.97×10^{-12}	0.77
3	270.7	529	0.96	1.20	0	1.97×10^{-12}	0.77
4	270.3	539	0.96	1.75	1	1.97×10^{-12}	0.77
5	270.3	545	0.96	2.48	8	1.97×10^{-12}	0.77
6	270.4	554	0.96	3.22	38	1.80×10^{-12}	0.75
7	270.3	567	0.96	3.90	116	1.50×10^{-12}	0.72
8	270.2	576	0.97	4.48	261	1.57×10^{-12}	0.73
9	270.2	591	0.97	4.96	475	9.83×10^{-13}	0.61
10	269.8	596	0.97	5.34	736	7.64×10^{-13}	0.53
11	269.9	605	0.97	5.63	1008	5.43×10^{-13}	0.42
12	269.7	610	0.97	5.84	1245	6.06×10^{-13}	0.45
13	269.6	625	0.97	5.96	1406	5.88×10^{-13}	0.44
14	269.8	643	0.97	6.00	1462	5.02×10^{-13}	0.40
15	269.1	659	0.97	5.96	1403	4.88×10^{-13}	0.40
16	268.7	681	0.97	5.83	1239	5.00×10^{-13}	0.40
17	268.1	706	0.97	5.62	1000	4.95×10^{-13}	0.40
18	268.4	740	0.97	5.33	727	5.00×10^{-13}	0.40
19	267.9	815	0.97	4.94	466	4.88×10^{-13}	0.40
20	267.2	884	0.97	4.45	254	5.05×10^{-13}	0.40
21	266.9	931	0.97	3.87	110	5.31×10^{-13}	0.41
22	267.5	962	0.98	3.18	35	5.84×10^{-13}	0.44
23	267.1	938	0.98	2.41	7	6.34×10^{-13}	0.77

S9 Concentration of aqueous species

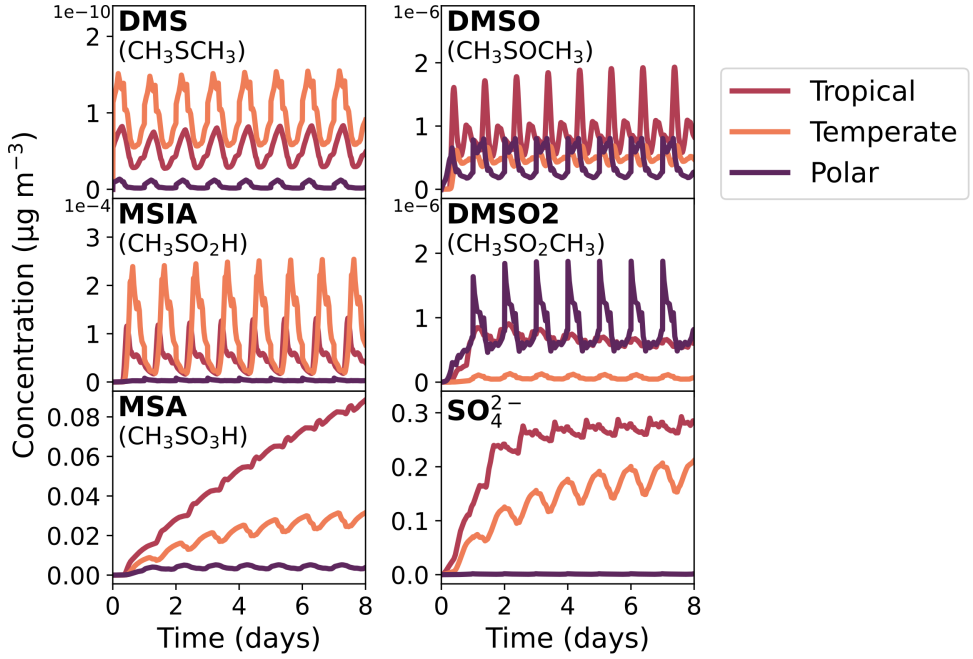

Figure S13. The concentration of DMS, DMSO, MSIA ($CH_3SO_2H/CH_3SO_2^-$), DMSO2, MSA ($CH_3SO_3H/CH_3SO_3^-$) and sulfate ($SO_4{}^{2-}$) partitioned into the aqueous phase across the three marine regimes. The concentrations provided are calculated using the volume of the full box (comprised of both air and aerosols).

S10 Exceptions to the uncertainty framework

There are a few exceptions to the application of the uncertainty framework, where the methodology cannot be applied, and the NASA panel report does not provide an uncertainty factor. These exceptions are described below.

For the reaction of CH_3SO with NO_2 two sets of products can form (CH_3 + SO_2 and CH_3SO_2), however, the NASA panel report only included the uncertainty for the total reaction (Burkholder et al., 2019). For that reaction, the uncertainty factor for the total reaction (1.44 at 2σ) was increased to account for the uncertainty in the branching ratio from Borissenko et al. (2003) (1.2 and 1.07 for the formation of SO_2 and CH_3SO_2, respectively).

Although the self-reaction of CH_3SCH_2OO (methylthiomethyl peroxy, MTMP) has been studied experimentally and given an uncertainty factor of 1.56 (Burkholder et al., 2019), following the MCM procedure, the reaction rate constant is combined with the measured CH_3OO rate constant ($f^2(T)$ = 1.44) to calculate a pooled RO_2 rate constant using double the geometric mean (as CH_3OO is the most abundant peroxy in the atmosphere) (Jenkin et al., 1997). Additionally, structure-activity relationships have been utilised to determine branching ratios for the peroxy self-reaction, increasing the associated uncertainty. For the pooled reaction between CH_3SCH_2OO and RO_2, an uncertainty factor of 3 was assigned.

Two studies measured the reaction of CH_3SCHO with OH radicals (Ye et al., 2022; Patroescu et al., 1996), and the rate constant determined was an average of the rate constant from both studies; an uncertainty factor of 1.5 was assigned as it provided an uncertainty range that included both measured rate constants and their associated uncertainty.

Although the reaction of CH_3SH and BrO has been measured directly, the experiments were performed at a low pressure (up to 3 Torr). Additionally, the reaction was found to show pressure dependence. As the rate constant at atmospheric pressures is unknown, the NASA panel report did not assign an uncertainty factor for the reaction, however, in this work we assigned an uncertainty factor of 10 to represent the pressure-related uncertainty.

In our mechanism, the rate constant for the addition of DMS with a Cl atom was calculated as the difference between the total rate constant for the reaction of DMS and Cl and the rate constant for the abstraction reaction. The NASA panel report provides uncertainty factors for both the total reaction and the abstraction, and the absolute errors calculated from the recommended uncertainty factors were combined to determine the relative uncertainty for the addition reaction.

Finally, for the equilibrium reactions of CH_3S, CH_3SO and CH_3SO_2 with oxygen, the uncertainty factor is attributed to the equilibrium rate constant. As the reactions with oxygen are sufficiently fast (due to the atmospheric concentrations of oxygen), only the uncertainty factor due to the equilibrium rate constant was considered, which was applied to the forward rate constant. The same methodology was applied to the reactions of $CH_3SO_2O_2$ and CH_3SOO_2 with NO_2, and the OH addition to DMS.

Uncertainties from Henry's law constants were also included. These uncertainty factors were based on the NASA panel report where available. In addition, a factor of 55 was used for the COSMO*therm* calculated constants from Wollesen de Jonge et al. (2021), and a factor of 100 was used for thioperformic acid (TPA), where no calculation had been performed. These larger rate constants represent the factors provided by the NASA panel report.

S11 Determining sample size

The sensitivity indices for four gas-phase species calculated from eight sets of Monte Carlo runs (covering 100, 250, 500, 1000, 1500, 2000, 2500 and 3000 simulations) for the tropical box model are shown in Figure S14. Only reactions with a sensitivity index higher than 0.05 in the 3000-run Monte Carlo set are shown. In Figure S14, the shaded area represents the largest negative sensitivity index calculated in the set; as Sobol sensitivity indices range from zero to one, negative sensitivity indices are considered noise due to model approximation error, however, large negative values indicate the sample size is too small.

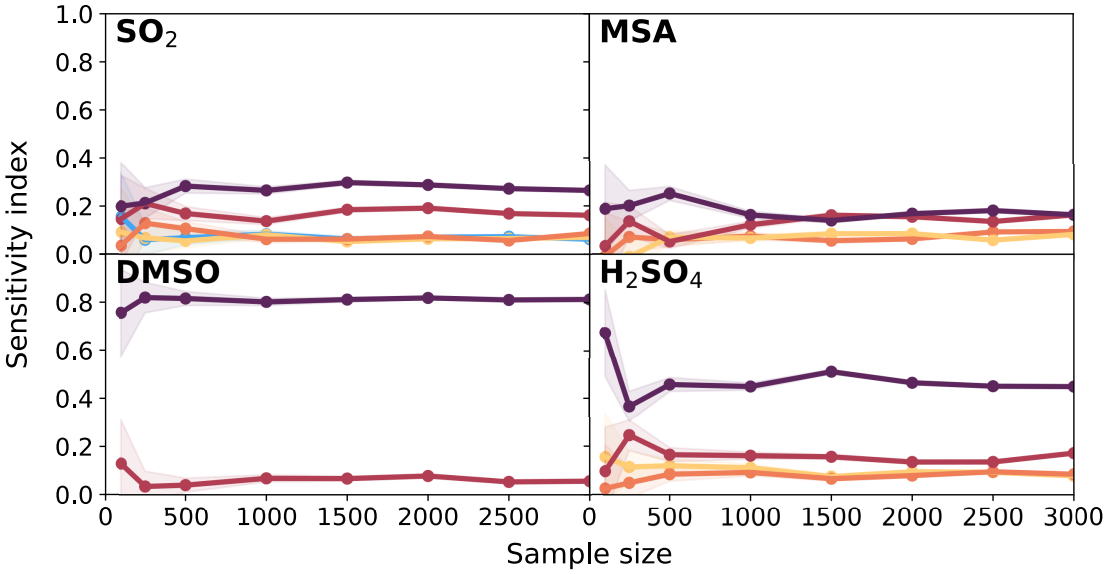

Figure S14. The sensitivity indices from different sets of Monte Carlo sample sizes for the reactions contributing the most to the uncertainty in gas-phase SO_2, MSA, DMSO and H_2SO_4 in the tropical box model at midday. Each line represents a reaction or process contributing to the uncertainty in the concentration of a species, with the colour of the line indicating the relative ranking of the reaction/process.

After 1000 runs, the sensitivity indices converged, however, the estimated sensitivity indices still showed some variation across the different sample sizes. This deviation is due to the variance in the sensitivity indices from resampling, with the mean representing the 'true' estimate from this method (Goffart and Woloszyn, 2021). Figure S15 demonstrates this variance in the resampling by showing the deviation from the mean in calculated sensitivity indices from sample sets that include 1000 runs or more, for reactions that have a sensitivity index of at least 0.05. This variance seems independent of the magnitude of the sensitivity index, and absolute values from one set of runs are generally within 0.04 of the mean.

For example, in the 2000 run simulation results for tropical box model, the most important contributor to the uncertainty in gas-phase SO_2, Henry's law constant for MSIA, has a sensitivity index of 0.287, which is within 0.04 of the mean sensitivity index for that process across the different sample sizes, 0.276. However, if only one set of runs were performed (with a sample size of 2000), the resulting sensitivity index could be described as 0.29 ± 0.04, to include the uncertainty due to running only

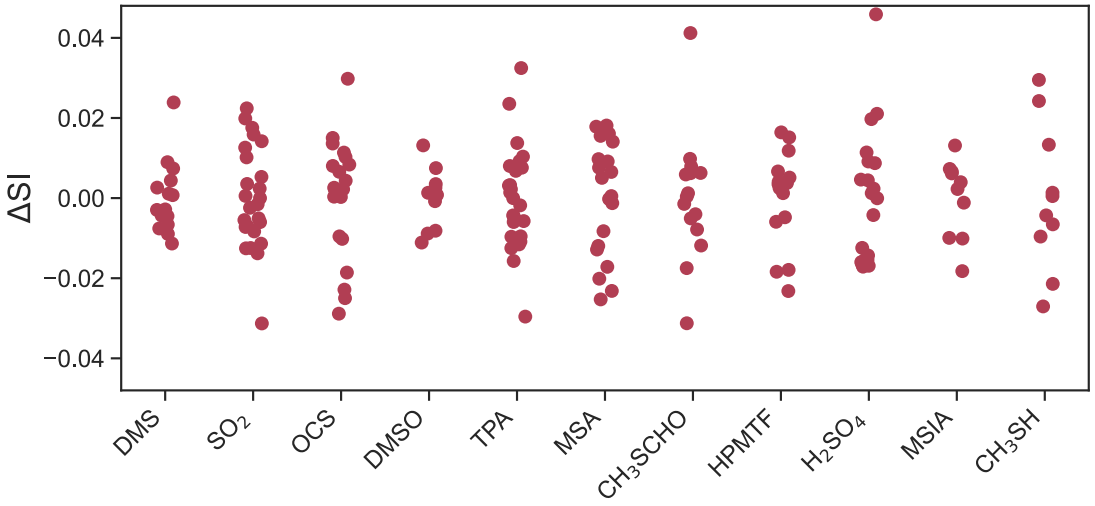

Figure S15. The deviation of the calculated sensitivity indices (ΔSI) of the 1000, 1500, 2000, 2500 and 3000 sample sets from their mean (for the most sensitive reactions in the tropical box model at midday), providing an absolute error from the variance in resampling.

one set of Monte Carlo simulations. This uncertainty does not account for the bias due to the estimation method, which may be higher (Azzini et al., 2021). For the temperate and polar box model runs only one set of Monte Carlo runs have been performed, with a sample size of 2000.

S12 Distribution in species concentrations

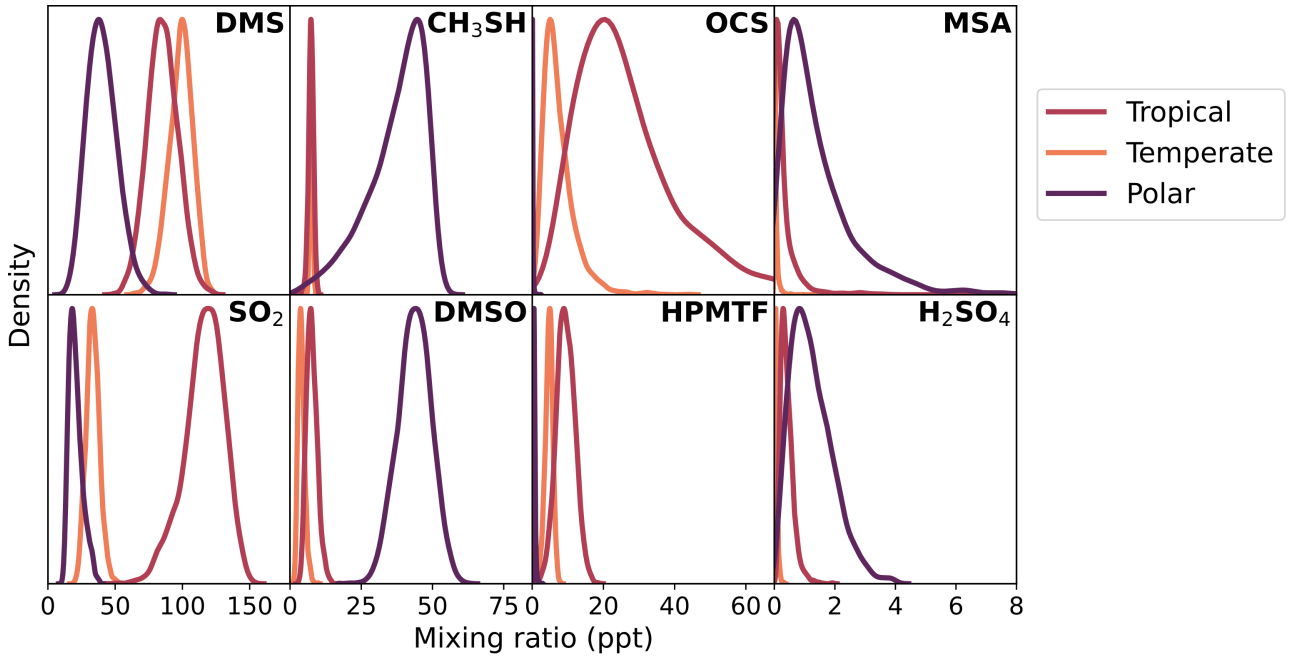

Figure S16. The distribution of midday gas-phase mixing ratios for DMS, CH_3SH, OCS, MSA, SO_2, DMSO, HPMTF and H_2SO_4 of the 2000 Monte Carlo simulations across the three marine regimes.

S13 Summary of sensitivity analysis at different times of the day

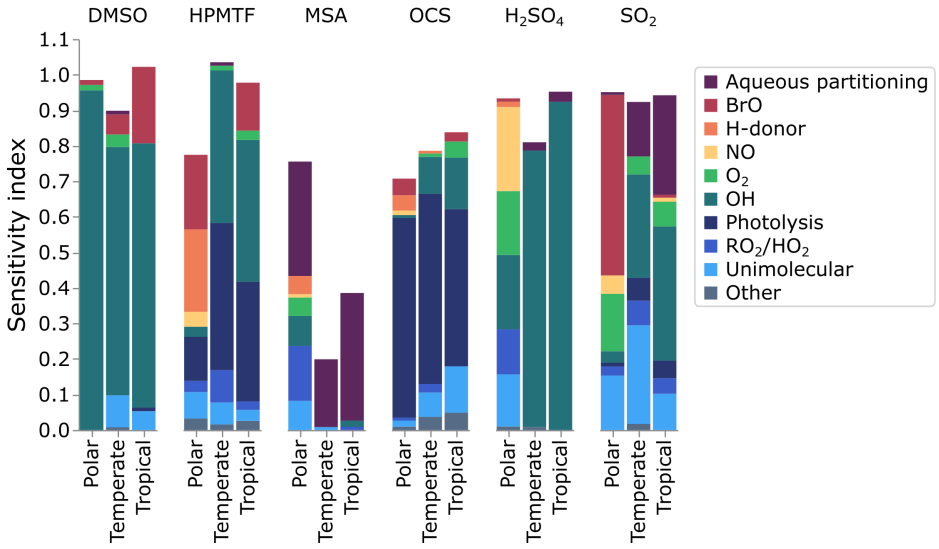

Figure S17. The contribution of different processes (reactions and phase transfers) to the uncertainty in gas-phase concentrations of DMSO, HPMTF, MSA, OCS, H_2SO_4 and SO_2 at midnight.

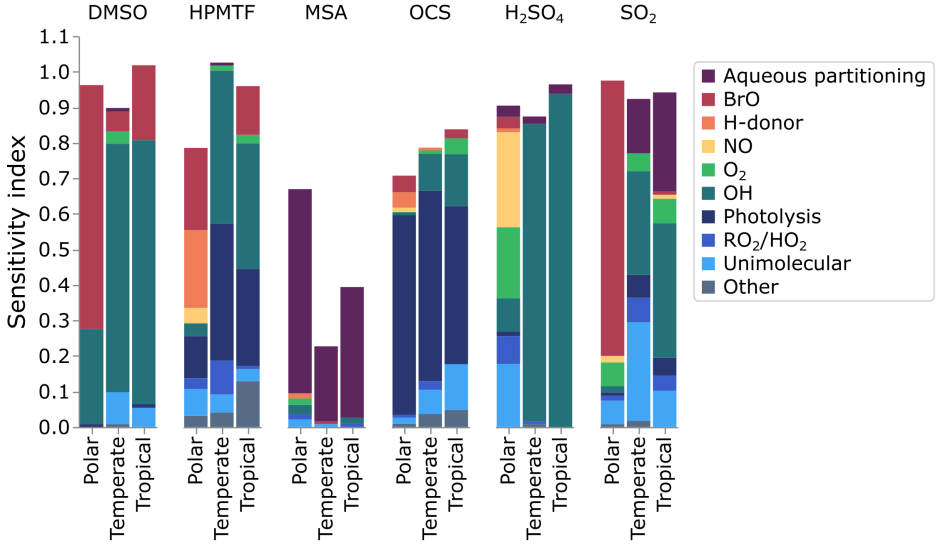

Figure S18. The contribution of different processes (reactions and phase transfers) to the uncertainty in gas-phase concentrations of DMSO, HPMTF, MSA, OCS, H_2SO_4 and SO_2 at 6 am.

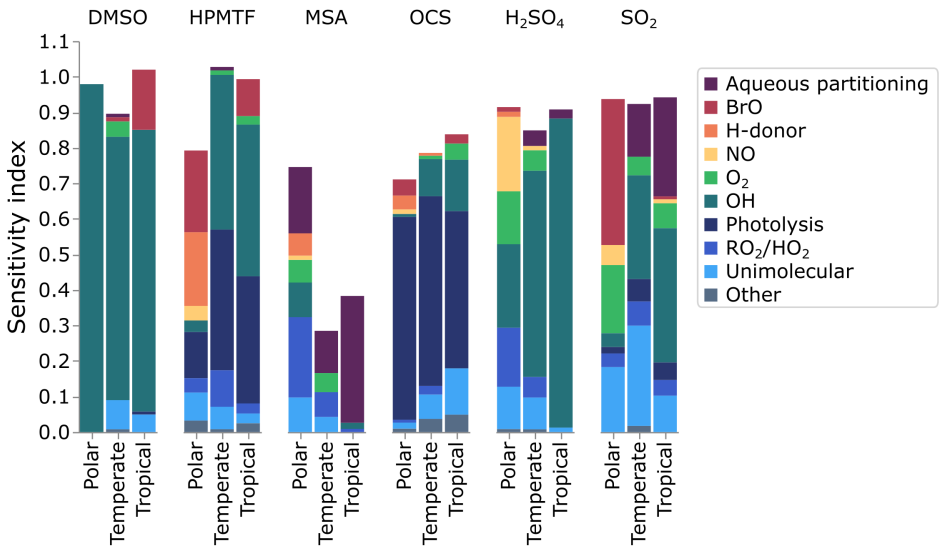

Figure S19. The contribution of different processes (reactions and phase transfers) to the uncertainty in gas-phase concentrations of DMSO, HPMTF, MSA, OCS, H_2SO_4 and SO_2 at 6 pm.

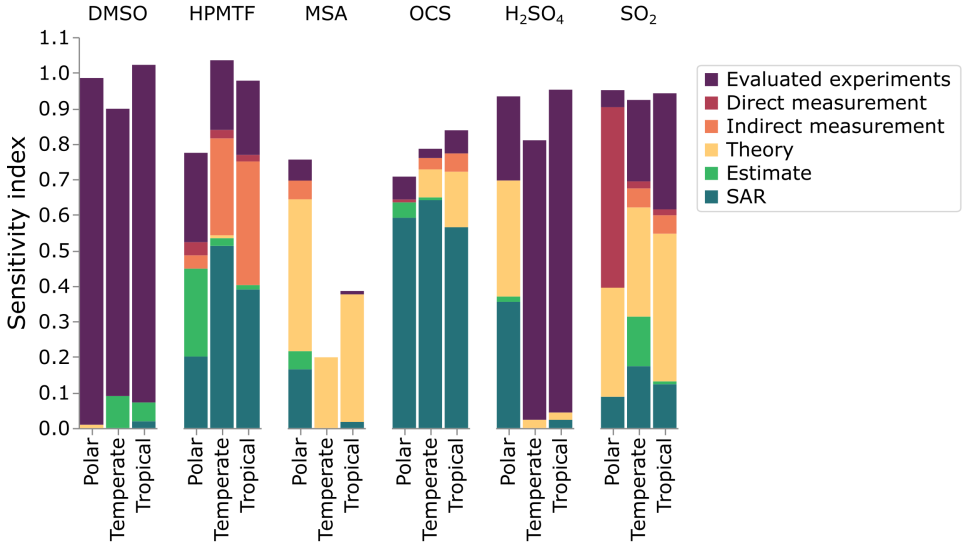

Figure S20. The contribution of different sources of rate constants to the uncertainty in gas-phase concentrations of DMSO, HPMTF, MSA, OCS, H_2SO_4 and SO_2 at midnight.

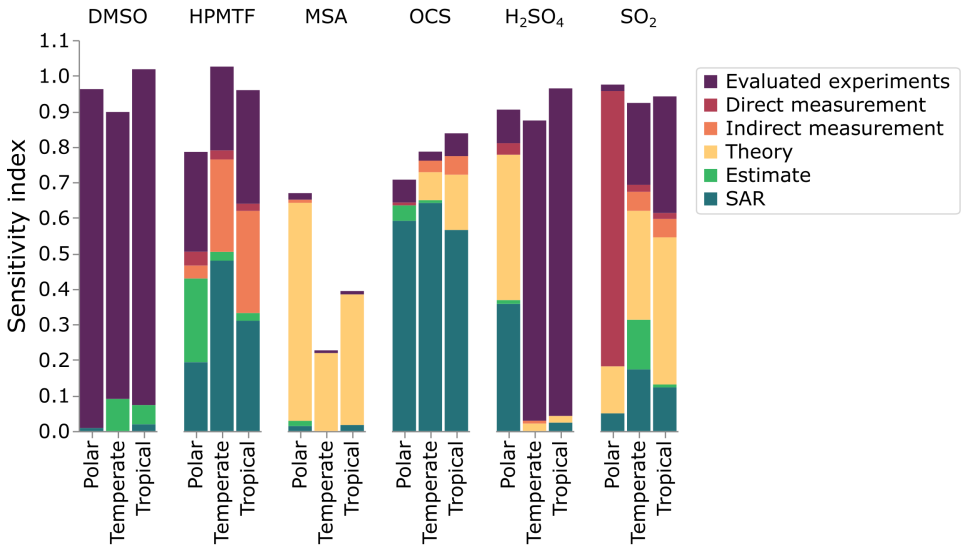

Figure S21. The contribution of different sources of rate constants to the uncertainty in gas-phase concentrations of DMSO, HPMTF, MSA, OCS, H_2SO_4 and SO_2 at 6 am.

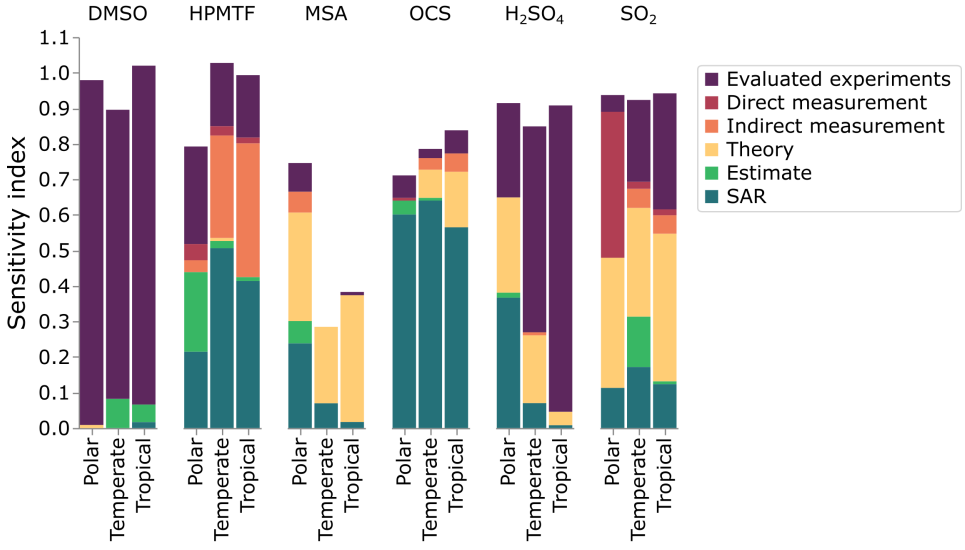

Figure S22. The contribution of different sources of rate constants to the uncertainty in gas-phase concentrations of DMSO, HPMTF, MSA, OCS, H_2SO_4 and SO_2 at 6 pm.

References

Albu, M., Barnes, I., Becker, K. H., Patroescu-Klotz, I., Benter, T., and Mocanu, R.: FT-IR Product Study on the OH Radical Initiated Oxidation of Dimethyl Sulfide: Temperature and O_2 Partial Pressure Dependence, in: Simulation and Assessment of Chemical Processes in a Multiphase Environment, edited by Barnes, I. and Kharytonov, M. M., pp. 501–513, Springer Science, Dortdrecht, https://doi.org/10.1007/978-1-4020-8846-9_41, 2008.

Allan, B., Ayers, G., Baker, J., Brough, N., Carpenter, L., Creasey, D., Fraser, P., Galbally, I., Gillett, R., Heard, D., Kivlighon, L., Kochhar, M., Krummel, P., Lee, J., Lewis, A., Meyer, M., Mills, G., Monks, P., Pilling, M., Salisbury, G., Steele, P., Sturrock, G., and Weeks, I.: Southern Ocean Atmospheric Photochemistry Experiment 2 (SOAPEX-2): atmospheric constituents concentration measurements from Cape Grim, Tasmania, NCAS British Atmospheric Data Centre, 30 July 2024. http://catalogue.ceda.ac.uk/uuid/a266f328ead407624dde4bb5c9e2e6a2/, 1987.

Andreae, M. O., Elbert, W., Cai, Y., Andrea, T. W., and Gras, J.: Non-sea-salt sulfate, methanesulfonate, and nitrate aerosol concentrations and size distributions at Cape Grim, Tasmania, J. Geophys. Res. Atmos., 104, 21 695–21 706, https://doi.org/10.1029/1999JD900283, 1999.

Arakaki, T., Anastasio, C., Kuroki, Y., Nakajima, H., Okada, K., Kotani, Y., Handa, D., Azechi, S., Kimura, T., Tsuhako, A., and Miyagi, Y.: A general scavenging rate constant for reaction of hydroxyl radical with organic carbon in atmospheric waters, Environ. Sci. Technol., 47, 8196–8203, https://doi.org/10.1021/es401927b, 2013.

Aranda, A., Diaz de Mera, Y., Rodrı´guez, D., Salgado, S., and Martinez, E.: Kinetic and products of the BrO+CH_3SH reaction: temperature and pressure dependence, Chem. Phys. Lett., 357, 471–476, https://doi.org/10.1016/S0009-2614(02)00561-4, 2002.

Atkinson, R., Baulch, D. L., Cox, R. A., Crowley, J. N., Hampson, R. F., Hynes, R. G., Jenkin, M. E., Rossi, M. J., and Troe, J.: Evaluated kinetic and photochemical data for atmospheric chemistry: volume I - gas phase reactions of O_x, HO_x, NO_x and SO_x species, Atmos. Chem. Phys., 4, 1461–1738, https://doi.org/10.5194/acp-4-1461-2004, 2004.

Azzini, I., Mara, T. A., and Rosati, R.: Comparison of two sets of Monte Carlo estimators of Sobol' indices, Environ. Model. Softw., 144, 105 167, https://doi.org/10.1016/j.envsoft.2021.105167, 2021.

Bauguitte, S. J.-B., Bloss, W. J., Evans, M. J., Salmon, R. A., Anderson, P. S., Jones, A. E., Lee, J. D., Saiz-Lopez, A., Roscoe, H. K., Wolff, E. W., and Plane, J. M. C.: Summertime NO_x measurements during the CHABLIS campaign: can source and sink estimates unravel observed diurnal cycles?, Atmos. Chem. Phys., 12, 989–1002, https://doi.org/10.5194/acp-12-989-2012, 2012.

Berndt, T.: Methanesulfonic acid (MSA) and SO_3 formation from the addition channel of atmospheric dimethyl sulfide oxidation, Chem. Commun., 61, 1443–1446, https://doi.org/10.1039/D4CC05913A, 2025.

Berndt, T., Hoffmann, E. H., Tilgner, A., Stratmann, F., and Herrmann, H.: Direct sulfuric acid formation from the gas-phase oxidation of reduced-sulfur compounds, Nat Commun, 14, 4849, https://doi.org/10.1038/s41467-023-40586-2, 2023.

Bloss, W. J., Lee, J. D., Heard, D. E., Salmon, R. A., Bauguitte, S. J.-B., Roscoe, H. K., and Jones, A. E.: Observations of OH and HO_2 radicals in coastal Antarctica, Atmos. Chem. Phys., 7, 4171–4185, https://doi.org/10.5194/acp-7-4171-2007, 2007.

Boniface, J., Shi, Q., Li, Y. Q., Cheung, J. L., Rattigan, O. V., Davidovits, P., Worsnop, D. R., Jayne, J. T., and Kolb, C. E.: Uptake of gas-phase SO_2, H_2S, and CO_2 by aqueous solutions, J. Phys. Chem. A, 104, 7502–7510, https://doi.org/10.1021/jp000479h, 2000.

Borissenko, D., Kukui, A., Laverdet, G., and Le Bras, G.: Experimental study of SO_2 formation in the reactions of CH_3SO radical with NO_2 and O_3 in relation with the atmospheric oxidation mechanism of dimethyl sulfide, J. Phys. Chem. A, 107, 1155–1161, https://doi.org/10.1021/jp021701g, 2003.

Burkholder, J. B., Sander, S. P., Abbatt, J. P. D., Barker, J. R., Cappa, C., Crounse, J. D., Dibble, T. S., Huie, R. E., Kolb, C. E., Kurylo, M. J., Orkin, V. L., Percival, C. J., Wilmouth, D. M., and Wine, P. H.: Chemical Kinetics and Photochemical Data for Use in Atmospheric Studies, Evaluation No. 19, Tech. rep., JPL Publication 19-5, Jet Propulsion Laboratory, Pasadena, http://jpldataeval.jpl.nasa.gov/, 2019.

Campolongo, F., Saltelli, A., Jensen, N. R., Wilson, J., and Hjorth, J.: The role of multiphase chemistry in the oxidation of dimethylsulphide (DMS). A latitude dependent analysis, J. Atmos. Chem., 32, 327–356, https://doi.org/10.1023/A:1006154618511, 1999.

Chen, J., Lane, J. R., Bates, K. H., and Kjaergaard, H. G.: Atmospheric gas-phase formation of methanesulfonic acid, Environ. Sci. Technol., 57, 21 168–21 177, https://doi.org/10.1021/acs.est.3c07120, 2023.

Chen, Q., Sherwen, T., Evans, M., and Alexander, B.: DMS oxidation and sulfur aerosol formation in the marine troposphere: a focus on reactive halogen and multiphase chemistry, Atmos. Chem. Phys., 18, 13 617–13 637, https://doi.org/10.5194/acp-18-13617-2018, 2018.

Clegg, S. L., Pitzer, K. S., and Brimblecombe, P.: Thermodynamics of multicomponent, miscible, ionic solutions. Mixtures including unsymmetrical electrolytes, J. Phys. Chem., 96, 9470–9479, https://doi.org/10.1021/j100202a074, 1992.

Clegg, S. L., Brimblecombe, P., and Wexler, A. S.: Thermodynamic model of the system H^+–NH_4^+–SO_4^{2-}–NO_3^-–H_2O at tropospheric temperatures, J. Phys. Chem. A, 102, 2137–2154, https://doi.org/10.1021/jp973042r, 1998.

De Bruyn, W. J., Shorter, J. A., Davidovits, P., Worsnop, D. R., Zahniser, M. S., and Kolb, C. E.: Uptake of gas phase sulfur species methanesulfonic acid, dimethylsulfoxide, and dimethyl sulfone by aqueous surfaces, J. Geophys. Res. Atmos., 99, 16 927–16 932, https://doi.org/10.1029/94JD00684, 1994.

Enami, S., Nakano, Y., Hashimoto, S., Kawasaki, M., Aloisio, S., and Francisco, J. S.: Reactions of Cl atoms with dimethyl sulfide: a theoretical calculation and an experimental study with cavity ring-down spectroscopy, J. Phys. Chem. A, 108, 7785–7789, https://doi.org/10.1021/jp049772y, 2004.

Ervens, B., George, C., Williams, J. E., Buxton, G. V., Salmon, G. A., Bydder, M., Wilkinson, F., Dentener, F., Mirabel, P., Wolke, R., and Herrmann, H.: CAPRAM 2.4 (MODAC mechanism): an extended and condensed tropospheric aqueous phase mechanism and its application, J. Geophys. Res. Atmos., 108, D144 426, https://doi.org/10.1029/2002JD002202, 2003.

Fomba, K. W., Müller, K., van Pinxteren, D., Poulain, L., van Pinxteren, M., and Herrmann, H.: Long-term chemical characterization of tropical and marine aerosols at the Cape Verde Atmospheric Observatory (CVAO) from 2007 to 2011, Atmos. Chem. Phys., 14, 8883–8904, https://doi.org/10.5194/acp-14-8883-2014, 2014.

Goffart, J. and Woloszyn, M.: EASI RBD-FAST: an efficient method of global sensitivity analysis for present and future challenges in building performance simulation, J. Build. Eng., 43, 103 129, https://doi.org/10.1016/j.jobe.2021.103129, 2021.

Goss, M. B. and Kroll, J. H.: Chamber studies of OH + dimethyl sulfoxide and dimethyl disulfide: insights into the dimethyl sulfide oxidation mechanism, Atmos. Chem. Phys., 24, 1299–1314, https://doi.org/10.5194/acp-24-1299-2024, 2024.

Hanson, D. R.: Mass accommodation of H_2SO_4 and CH_3SO_3H on water-sulfuric acid solutions from 6% to 97% RH, J. Phys. Chem. A, 109, 6919–6927, https://doi.org/10.1021/jp0510443, 2005.

Hersbach, H., Bell, B., Berrisford, P., Biavati, G., Horányi, A., Muñoz Sabater, J., Nicolas, J., Peubey, C., Radu, R., Rozum, I., Schepers, D., Simmons, A., Soci, C., Dee, D., and Thépaut, J.-N.: ERA5 hourly data on single levels from 1940 to present, copernicus Climate Change Service (C3S) Climate Data Store (CDS), 30 Oct 2024. 10.24381/cds.adbb2d47, 2023.

Hicks, B. B., Baldocchi, D. D., Meyers, T. P., Hosker, R. P., and Matt, D. R.: A preliminary multiple resistance routine for deriving dry deposition velocities from measured quantities, Water Air Soil Pollut., 36, 311–330, https://doi.org/10.1007/BF00229675, 1987.

Hoffmann, E. H., Tilgner, A., Schrödner, R., Bräuer, P., Wolke, R., and Herrmann, H.: An advanced modeling study on the impacts and atmospheric implications of multiphase dimethyl sulfide chemistry, Proc. Natl. Acad. Sci. U.S.A., 113, 11 776–11 781, https://doi.org/10.1073/pnas.1606320113, 2016.

Jacob, L. S. D., Giorio, C., and Archibald, A. T.: Extension, development, and evaluation of the representation of the OH-initiated dimethyl sulfide (DMS) oxidation mechanism in the Master Chemical Mechanism (MCM) v3.3.1 framework, Atmos. Chem. Phys., 24, 3329–3347, https://doi.org/10.5194/acp-24-3329-2024, 2024.

Jenkin, M. E., Saunders, S. M., and Pilling, M. J.: The tropospheric degradation of volatile organic compounds: a protocol for mechanism development, Atmos. Environ., 31, 81–104, https://doi.org/10.1016/S1352-2310(96)00105-7, 1997.

Jernigan, C. M., Fite, C. H., Vereecken, L., Berkelhammer, M. B., Rollins, A. W., Rickly, P. S., Novelli, A., Taraborrelli, D., Holmes, C. D., and Bertram, T. H.: Efficient production of carbonyl sulfide in the low-NO_x oxidation of dimethyl sulfide, Geophys. Res. Lett., 49, e2021GL096 838, https://doi.org/10.1029/2021GL096838, 2022.

Jernigan, C. M., Rivard, M. J., Berkelhammer, M. B., and Bertram, T. H.: Sulfate and carbonyl sulfide production in aqueous reactions of hydroperoxymethyl thioformate, ACS ES&T Air, 1, 397–404, https://doi.org/10.1021/acsestair.3c00098, 2024.

Jones, A. E., Wolff, E. W., Salmon, R. A., Bauguitte, S. J.-B., Roscoe, H. K., Anderson, P. S., Ames, D., Clemitshaw, K. C., Fleming, Z. L., Bloss, W. J., Heard, D. E., Lee, J. D., Read, K. A., Hamer, P., Shallcross, D. E., Jackson, A. V., Walker, S. L., Lewis, A. C., Mills, G. P., Plane, J. M. C., Saiz-Lopez, A., Sturges, W. T., and Worton, D. R.: Chemistry of the Antarctic Boundary Layer and the Interface with Snow: an overview of the CHABLIS campaign, Atmos. Chem. Phys., 8, 3789–3803, https://doi.org/10.5194/acp-8-3789-2008, 2008.

Knote, C. and Barre, J.: BOXMOX extension to KPP, available at: https://mbees.med.uni-augsburg.de/boxmodeling/ (last access: March 2025), 2022.

Lee, J. D., McFiggans, G., Allan, J. D., Baker, A. R., Ball, S. M., Benton, A. K., Carpenter, L. J., Commane, R., Finley, B. D., Evans, M., Fuentes, E., Furneaux, K., Goddard, A., Good, N., Hamilton, J. F., Heard, D. E., Herrmann, H., Hollingsworth, A., Hopkins, J. R., Ingham, T., Irwin, M., Jones, C. E., Jones, R. L., Keene, W. C., Lawler, M. J., Lehmann, S., Lewis, A. C., Long, M. S., Mahajan, A., Methven, J., Moller, S. J., Müller, K., Müller, T., Niedermeier, N., O'Doherty, S., Oetjen, H., Plane, J. M. C., Pszenny, A. A. P., Read, K. A., Saiz-Lopez, A., Saltzman, E. S., Sander, R., von Glasow, R., Whalley, L., Wiedensohler, A., and Young, D.: Reactive halogens in the marine boundary layer (RHaMBLe): the tropical North Atlantic experiments, Atmos. Chem. Phys., 10, 1031–1055, https://doi.org/10.5194/acp-10-1031-2010, 2010.

Magi, L., Schweitzer, F., Pallares, C., Cherif, S., Mirabel, P., and George, C.: Investigation of the uptake rate of ozone and methyl hydroperoxide by water surfaces, J. Phys. Chem. A, 101, 4943–4949, https://doi.org/10.1021/jp970646m, 1997.

Millero, F. J.: Atmospheric Chemistry, in: Chemical Oceanography, chap. 5, p. 220, CRC Press, Boca Raton, Florida, third edition edn., 2013.

Müller, K., Lehmann, S., van Pinxteren, D., Gnauk, T., Niedermeier, N., Wiedensohler, A., and Herrmann, H.: Particle characterization at the Cape Verde atmospheric observatory during the 2007 RHaMBLe intensive, Atmos. Chem. Phys., 10, 2709–2721, https://doi.org/10.5194/acp-10-2709-2010, 2010.

Natural Environment Research Council, Bauguitte, S., Bloss, W., Clemitshaw, K., Fleming, Z., Heard, D., Jackson, A., Jones, A., Lee, J., Lewis, A., Mills, G., Rankin, A., Read, K., Roscoe, H., Salmon, R., Walker, S., and Wolff, E.: Chemistry of the Antarctic Boundary Layer and the Interface with Snow (CHABLIS): meteorological and atmospheric chemistry field measurements, NCAS British Atmospheric Data Centre, 30 July 2024. http://catalogue.ceda.ac.uk/uuid/6a5cf2c6e142975e71ff340e0c41777d/, 2005.

Natural Environment Research Council, Whalley, L., Pszenny, A., and Keene, W.: Reactive halogens in the marine boundary layer (RHaMBLe) campaign at Cape Verde (2007), NCAS British Atmospheric Data Centre, 30 July 2024. http://catalogue.ceda.ac.uk/uuid/a2d86deca5264e38bce22b8c96f01d99/, 2006.

Patroescu, I. V., Barnes, I., and Becker, K. H.: FTIR kinetic and mechanistic study of the atmospheric chemistry of methyl thiolformate, J. Phys. Chem., 100, 17 207–17 217, https://doi.org/10.1021/jp961452u, 1996.

Peng, C., Chen, L., and Tang, M.: A database for deliquescence and efflorescence relative humidities of compounds with atmospheric relevance, Fundam. Res., 2, 578–587, https://doi.org/10.1016/j.fmre.2021.11.021, 2022.

Ranjithkumar, A., Gordon, H., Williamson, C., Rollins, A., Pringle, K., Kupc, A., Abraham, N. L., Brock, C., and Carslaw, K.: Constraints on global aerosol number concentration, SO_2 and condensation sink in UKESM1 using ATom measurements, Atmos. Chem. Phys., 21, 4979–5014, https://doi.org/10.5194/acp-21-4979-2021, 2021.

Read, K. A., Lewis, A. C., Bauguitte, S., Rankin, A. M., Salmon, R. A., Wolff, E. W., Saiz-Lopez, A., Bloss, W. J., Heard, D. E., Lee, J. D., and Plane, J. M. C.: DMS and MSA measurements in the Antarctic Boundary Layer: impact of BrO on MSA production, Atmos. Chem. Phys., 8, 2985–2997, https://doi.org/10.5194/acp-8-2985-2008, 2008.

Saiz-Lopez, A., Mahajan, A. S., Salmon, R. A., Bauguitte, S. J.-B., Jones, A. E., Roscoe, H. K., and Plane, J. M. C.: Boundary layer halogens in coastal Antarctica, Science, 317, 348–351, https://doi.org/10.1126/science.1141408, 2007.

Salmon, R. A., Bauguitte, S. J.-B., Bloss, W., Hutterli, M. A., Jones, A. E., Read, K., and Wolff, E. W.: Measurement and interpretation of gas phase formaldehyde concentrations obtained during the CHABLIS campaign in coastal Antarctica, Atmos. Chem. Phys., 8, 4085–4093, https://doi.org/10.5194/acp-8-4085-2008, 2008.

Sander, R., Pszenny, A. A. P., Keene, W. C., Crete, E., Deegan, B., Long, M. S., Maben, J. R., and Young, A. H.: Gas phase acid, ammonia and aerosol ionic and trace element concentrations at Cape Verde during the Reactive Halogens in the Marine Boundary Layer (RHaMBLe) 2007 intensive sampling period, Earth Syst. Sci. Data, 5, 385–392, https://doi.org/10.5194/essd-5-385-2013, 2013.

Sandu, A. and Sander, R.: Technical note: Simulating chemical systems in Fortran90 and Matlab with the Kinetic PreProcessor KPP-2.1, Atmos. Chem. Phys., 6, 187–195, https://doi.org/10.5194/acp-6-187-2006, 2006.

Shen, J., Scholz, W., He, X.-C., Zhou, P., Marie, G., Wang, M., Marten, R., Surdu, M., Rörup, B., Baalbaki, R., Amorim, A., Ataei, F., Bell, D. M., Bertozzi, B., Brasseur, Z., Caudillo, L., Chen, D., Chu, B., Dada, L., Duplissy, J., Finkenzeller, H., Granzin, M., Guida, R., Heinritzi, M., Hofbauer, V., Iyer, S., Kemppainen, D., Kong, W., Krechmer, J. E., Kürten, A., Lamkaddam, H., Lee, C. P., Lopez, B., Mahfouz, N. G. A., Manninen, H. E., Massabò, D., Mauldin, R. L., Mentler, B., Müller, T., Pfeifer, J., Philippov, M., Piedehierro, A. A., Roldin, P., Schobesberger, S., Simon, M., Stolzenburg, D., Tham, Y. J., Tomé, A., Umo, N. S., Wang, D., Wang, Y., Weber, S. K., Welti, A., Wollesen de Jonge, R., Wu, Y., Zauner-Wieczorek, M., Zust, F., Baltensperger, U., Curtius, J., Flagan, R. C., Hansel, A., Möhler, O., Petäjä, T., Volkamer, R., Kulmala, M., Lehtipalo, K., Rissanen, M., Kirkby, J., El-Haddad, I., Bianchi, F., Sipilä, M., Donahue, N. M., and Worsnop, D. R.: High gas-phase methanesulfonic acid production in the OH-initiated oxidation of dimethyl sulfide at low temperatures, Environ. Sci. Technol., 56, 13 931–13 944, https://doi.org/10.1021/acs.est.2c05154, 2022.

Sommariva, R., Haggerstone, A.-L., Carpenter, L. J., Carslaw, N., Creasey, D. J., Heard, D. E., Lee, J. D., Lewis, A. C., Pilling, M. J., and Zádor, J.: OH and HO_2 chemistry in clean marine air during SOAPEX-2, Atmos. Chem. Phys., 4, 839–856, https://doi.org/10.5194/acp-4-839-2004, 2004.

Tang, M. J., Cox, R. A., and Kalberer, M.: Compilation and evaluation of gas phase diffusion coefficients of reactive trace gases in the atmosphere: volume 1. Inorganic compounds, Atmos. Chem. Phys., 14, 9233–9247, https://doi.org/10.5194/acp-14-9233-2014, 2014.

Urbanski, S. P. and Wine, P. H.: Spectroscopic and kinetic study of the $Cl\text{-}S(CH_3)_2$ adduct, J. Phys. Chem. A, 103, 10 935–10 944, https://doi.org/10.1021/jp992682m, 1999.

Vereecken, L., Novelli, A., Taraborrelli, D., and Wahner, A.: Perhemiacetal formation and Cl/NO_3-initiated chemistry of hydroperoxymethylthioformate (HPMTF) in atmospheric DMS oxidation, Environ. Sci.: Atmos., 5, 181–190, https://doi.org/10.1039/D4EA00134F, 2025.

Veres, P. R., Andrew Neuman, J., Bertram, T. H., Assaf, E., Wolfe, G. M., Williamson, C. J., Weinzierl, B., Tilmes, S., Thompson, C. R., Thames, A. B., Schroder, J. C., Saiz-Lopez, A., Rollins, A. W., Roberts, J. M., Price, D., Peischl, J., Nault, B. A., Møller, K. H., Miller, D. O., Meinardi, S., Li, Q., Lamarque, J. F., Kupc, A., Kjaergaard, H. G., Kinnison, D., Jimenez, J. L., Jernigan, C. M., Hornbrook, R. S., Hills, A., Dollner, M., Day, D. A., Cuevas, C. A., Campuzano-Jost, P., Burkholder, J., Paul Bui, T., Brune, W. H., Brown, S. S., Brock, C. A., Bourgeois, I., Blake, D. R., Apel, E. C., and Ryerson, T. B.: Global airborne sampling reveals a previously unobserved dimethyl sulfide oxidation mechanism in the marine atmosphere, Proc. Natl. Acad. Sci. U.S.A., 117, 4505–4510, https://doi.org/10.1073/pnas.1919344117, 2020.

Watts, S. F. and Brimblecombe, P.: The Henry's law constant of dimethyl sulphoxide, Environ. Tech. Lett., 8, 483–486, https://doi.org/10.1080/09593338709384509, 1987.

Wesely, M.: Parameterization of surface resistances to gaseous dry deposition in regional-scale numerical models, Atmos. Environ., 23, 1293–1304, https://doi.org/10.1016/0004-6981(89)90153-4, 1989.

Wexler, A. S.: Atmospheric aerosol models for systems including the ions H^+, NH_4^+, Na^+, SO_4^{2-}, NO_3^-, Cl^-, Br^-, and H_2O, J. Geophys. Res. Atmos., 107, D144 207, https://doi.org/10.1029/2001JD000451, 2002.

Wofsy, S., Afshar, S., Allen, H., Apel, E., Asher, E., Barletta, B., Bent, J., Bian, H., Biggs, B., Blake, D., Blake, N., Bourgeois, I., Brock, C., Brune, W., Budney, J., Bui, T., Butler, A., Campuzano-Jost, P., Chang, C., Chin, M., Commane, R., Correa, G., Crounse, J., Cullis, P. D., Daube, B., Day, D., Dean-Day, J., Dibb, J., DiGangi, J., Diskin, G., Dollner, M., Elkins, J., Erdesz, F., Fiore, A., Flynn, C., Froyd, K., Gesler, D., Hall, S., Hanisco, T., Hannun, R., Hills, A., Hintsa, E., Hoffman, A., Hornbrook, R., Huey, L., Hughes, S., Jimenez, J., Johnson, B., Katich, J., Keeling, R., Kim, M., Kupc, A., Lait, L., Lamarque, J.-F., Liu, J., McKain, K., Mclaughlin, R., Meinardi, S., Miller, D., Montzka, S., Moore, F., Morgan, E., Murphy, D., Murray, L., Nault, B., Neuman, J., Newman, P., Nicely, J., Pan, X., Paplawsky, W., Peischl, J., Prather, M., Price, D., Ray, E., Reeves, J., Richardson, M., Rollins, A., Rosenlof, K., Ryerson, T., Scheuer, E., Schill, G., Schroder, J., Schwarz, J., St.Clair, J., Steenrod, S., Stephens, B., Strode, S., Sweeney, C., Tanner, D., Teng, A., Thames, A., Thompson, C., Ullmann, K., Veres, P., Vieznor, N., Wagner, N., Watt, A., Weber, R., Weinzierl, B., Wennberg, P., Williamson, C., Wilson, J., Wolfe, G., Woods, C., and Zeng, L.: ATom: merged atmospheric chemistry, trace gases, and aerosols, https://doi.org/10.3334/ORNLDAAC/1581, ORNL Distributed Active Archive Center, 12 Jan 2025. https://daac.ornl.gov/cgi-bin/dsviewer.pl?ds_id=1581.

Wolke, R., Sehili, A., Simmel, M., Knoth, O., Tilgner, A., and Herrmann, H.: SPACCIM: a parcel model with detailed microphysics and complex multiphase chemistry, Atmos. Environ., 39, 4375–4388, https://doi.org/10.1016/j.atmosenv.2005.02.038, 2005.

Wollesen de Jonge, R., Elm, J., Rosati, B., Christiansen, S., Hyttinen, N., Lüdemann, D., Bilde, M., and Roldin, P.: Secondary aerosol formation from dimethyl sulfide – improved mechanistic understanding based on smog chamber experiments and modelling, Atmos. Chem. Phys, 21, 9955–9976, https://doi.org/10.5194/acp-21-9955-2021, 2021.

Ye, Q., Goss, M. B., Krechmer, J. E., Majluf, F., Zaytsev, A., Li, Y., Roscioli, J. R., Canagaratna, M., Keutsch, F. N., Heald, C. L., and Kroll, J. H.: Product distribution, kinetics, and aerosol formation from the OH oxidation of dimethyl sulfide under different RO_2 regimes, Atmos. Chem. Phys., 22, 16 003–16 015, https://doi.org/10.5194/acp-22-16003-2022, 2022.

Yin, F., Grosjean, D., and Seinfeld, J. H.: Photooxidation of dimethyl sulfide and dimethyl disulfide part I: mechanism development, J. Atmos. Chem., 11, 309–364, https://doi.org/10.1007/BF00053780, 1990.

Zhang, L., Brook, J. R., and Vet, R.: A revised parameterization for gaseous dry deposition in air-quality models, Atmos. Chem. Phys., 3, 2067–2082, https://doi.org/10.5194/acp-3-2067-2003, 2003.

Zhu, L., Nenes, A., Wine, P. H., and Nicovich, J. M.: Effects of aqueous organosulfur chemistry on particulate methanesulfonate to non–sea salt sulfate ratios in the marine atmosphere, J. Geophys. Res. Atmos., 111, D05 316, https://doi.org/10.1029/2005JD006326, 2006.